Delft University of Technology

FE-assisted investigation for mechanical behaviour of connections in offshore wind turbine towers

Cheng, Lu; Yang, Fei; Seidel, Marc; Veljkovic, Milan

DOI
10.1016/j.engstruct.2023.116039

Publication date
2023

Document Version
Final published version

Published in
Engineering Structures

Citation (APA)
Cheng, L., Yang, F., Seidel, M., & Veljkovic, M. (2023). FE-assisted investigation for mechanical behaviour of connections in offshore wind turbine towers. *Engineering Structures*, *285*, Article 116039. https://doi.org/10.1016/j.engstruct.2023.116039

Important note
To cite this publication, please use the final published version (if applicable).
Please check the document version above.

Copyright
Other than for strictly personal use, it is not permitted to download, forward or distribute the text or part of it, without the consent of the author(s) and/or copyright holder(s), unless the work is under an open content license such as Creative Commons.

Takedown policy
Please contact us and provide details if you believe this document breaches copyrights.
We will remove access to the work immediately and investigate your claim.

This work is downloaded from Delft University of Technology.
For technical reasons the number of authors shown on this cover page is limited to a maximum of 10.

Engineering Structures 285 (2023) 116039

Contents lists available at ScienceDirect

Engineering Structures

journal homepage: www.elsevier.com/locate/engstruct

FE-assisted investigation for mechanical behaviour of connections in offshore wind turbine towers

Lu Cheng [a,*], Fei Yang [b], Marc Seidel [c], Milan Veljkovic [a]

[a] Faculty of Civil Engineering and Geosciences, Delft University of Technology, Delft, the Netherlands
[b] School of Civil Engineering, Chang'an University, Xi'an, China
[c] Siemens Gamesa Renewable Energy GmbH & Co. KG, Hamburg, Germany

ARTICLE INFO

Keywords:
Ring flange connection
C1 wedge connection
Finite element analysis
Tensile behaviour
Fatigue performance
Wind turbine tower

ABSTRACT

The overall competitiveness of offshore wind turbine towers is significantly influenced by the selection of the connection. The following three types of connections: a conventional bolted ring flange (RF) connection, ring flange connection with defined contact surfaces (RFD), and C1 wedge connection (C1-WC) are considered. A quantitative comparison is made to enhance performance in a specific condition and enable further optimization of these connections in engineering practices. The study compares the tensile behaviour and fatigue performance of these connections by validated finite element (FE) simulation and analysis. The proposed FE modelling is based on a realistic geometry including all contacts present in the connections, steel full-range stress–strain relationship and ductile damage model. The efficiency and accuracy of the FE models are validated through the comparison with the performed tests. Then, a series of parametric FE analyses are carried out to examine the impact of the applied boundary conditions, bolt pretension level, and steel grade on the behaviour of connections. Load-displacement curves, bolt evolution curves, and stress responses are analysed to compare their tensile behaviour. The effectiveness of conventional segment specimen testing is evaluated thoroughly. For the fatigue performance of connections, the results indicate that the segment specimen testing substantially underestimates the fatigue performance of C1-WCs. This discrepancy is essential to be considered in the tower design. It is also noted that C1-WCs are rather insensitive to the variation of pretension force level, which show superiority to avoiding the difficulties associated with typically bolted joints. This research provides in-depth knowledge for the practical application of such connections and further optimization.

1. Introduction

Wind power has been one of the most affordable methods in terms of renewable electric energy supply and carbon emissions reduction [1–3]. A wind farm is primarily made up of a collection of wind turbines, which are placed in certain locations on land or in sea to harvest the onshore or offshore wind energy. Onshore wind farms are noted for being affordable and quick to install, while they generate less power due to lower average wind speeds. In contrast, by exploiting powerful and more consistent offshore winds, offshore wind farms (OWFs) ensure generation of electrical energy with fewer negative environmental impacts [4,5]. Over the past decade, the offshore wind industry in Europe has grown rapidly. Europe now has 28.4 GW of installed offshore capacity, which rose by almost 56 % annually from 2011 to 2022 [6,7]. Fig. 1 shows the growth of OWFs in Europe since 2011 with aspects of installed capacity, size, and locations. The average rated capacity of turbines and OWF size in 2021 are 2.4 and 2.2 times of that in 2011, respectively. Before 2013, there was no OWF located further away than 50 km off the shore [7]. After that, the average water depth and distance to the coast show an increasing trend, as well as the average OWF size. The average distance in recent years has fallen because fewer projects are built at a greater distance.

According to the size of the turbine, the depth of the water, and the geotechnical conditions, five types of foundations are frequently utilized in OWF projects (see Fig. 2). Among them, the monopile (MP) foundation, which now totals 4914 units, continues to be the most popular foundation type (82 %) [8]. Its predominance can be attributed to its ease of design and simple installation and delivery procedures. For OWFs with a water depth of 0–30 m, a monopile foundation offers benefits in terms of economics and technology. A transition piece (TP) is

---

* Corresponding author.
E-mail address: L.cheng-2@tudelft.nl (L. Cheng).

https://doi.org/10.1016/j.engstruct.2023.116039

Available online 1 April 2023
0141-0296/© 2023 The Author(s). Published by Elsevier Ltd. This is an open access article under the CC BY license (http://creativecommons.org/licenses/by/4.0/).

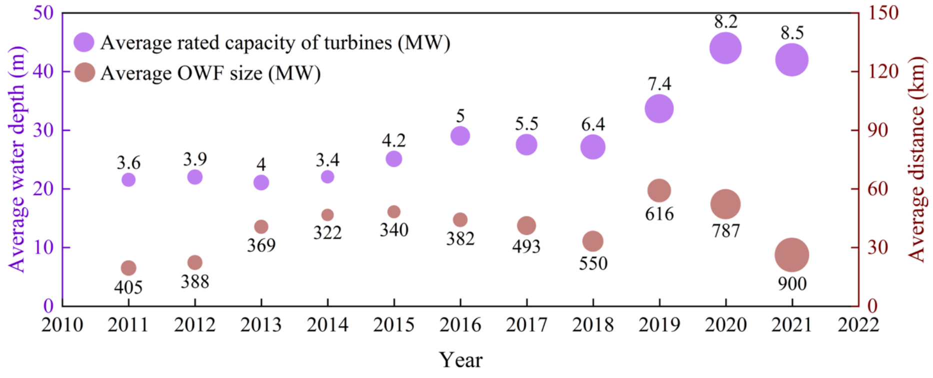

Fig. 1. Development of OWFs in terms of average water depth and rated capacity of turbines (violet), and average distance to coast and OWF size (brown) in Europe. (For interpretation of the references to color in this figure legend, the reader is referred to the web version of this article.)

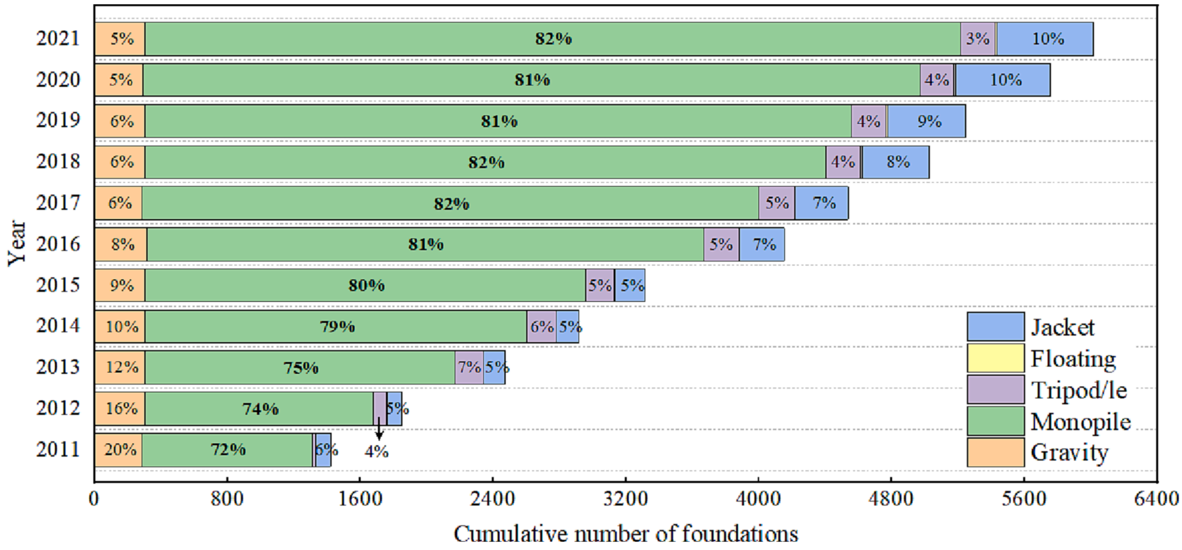

Fig. 2. Share of foundation types of OWF projects in Europe [5,7,8].

then attached to the top of the installed pile by connections after driving the monopiles into the seabed.

Currently, OWFs with rather large wind turbines positioned at depths more than 30 m also adopt monopile substructures [9], where large-diameter monopiles are required to guarantee structural stiffness. Given that wind speed tends to increase as height increases, turbine towers are likewise getting taller to harvest more energy. Such huge diameters and heights result in exponentially rising costs. The connections between TP and MP are consequently subjected to much larger forces and moments. In addition, the harsh offshore environment also increases the risk of fatigue failure to the connections. Therefore, to ensure the excellent structural performance of OWFs, it is essential to design more reliable TP-MP connections. In recent years, several alternatives are proposed, which include bolted ring-flange (RF) connections [10–13], ring-flange connections with defined contacts (RFD) [10,14], and C1 wedge connections (WCs) [15,16].

Among these connections, the bolted ring-flange (RF) connection, the most popular for the MP-TP connection, is utilized extensively in the most recent OWT projects in Europe, such as Nobel wind Offshore Wind Farm [17]. By utilizing the conventional segment approach, analytical models and design principles have been proposed for this connection [10,11]. The Schmidt/Neuper model [18] is most widely used for fatigue limit states (FLS) assessment and Petersen/Seidel model [11,19] for ultimate limit states (ULS). Standard design procedures are provided by guidelines and codes, including (a) DNVGL-ST-0126 [20]; (b) DIN 18088–3 [21]; (c) [22] VDI 2230 Part I; (d) IEC 61400–6 [23]; (e) RP-C203 [24]. The ULS and FLS conditions are two essentials for RF connection design. The overall resistance of RF connections is strongly linked to the used high-strength bolt behaviour [25–27].

In contrast to RF connection [11], RFD connection is a concept which shows favourable fatigue performance. Krutschinna [14] provided an analytical model to evaluate the bolt force evolution in RFD connections via pretty refined FE analyses. The comparison of the mechanical behaviour between RF and RFD connections with different bolt types was highlighted in [28]. Although the benefits of fatigue endurance were proven, there has only been a relatively small amount of implementation of this connection in practice yet. It should be noted that the behaviour of RF and RFD connections is dominantly dependent on bolt resistance. The bolt assembly is under combined tension and bending loads due to the eccentricity between the tower segment and bolts in RF/RFD connections.

The C1-WC was designed by the company of C1 Connections B.V. [15,16] in early 2017. The details about the geometry and assembly procedure are described in [29]. Extensive FE analyses, ultimate capacity tests, and a series of fatigue segment testing have been conducted by C1 Connections B.V. and TU Delft. It is concluded that the C1-WC is a competitive option with high capacity, low expense, and fast installation. The remarkable improvement is that the load from the upper to lower tower segment is transferred centrically between the segments. The required bolt size for such centric connection is much smaller than in RF/RFD connections. The variation of bolt force is almost negligible under service loads, and the bolt is still in an elastic state at ultimate

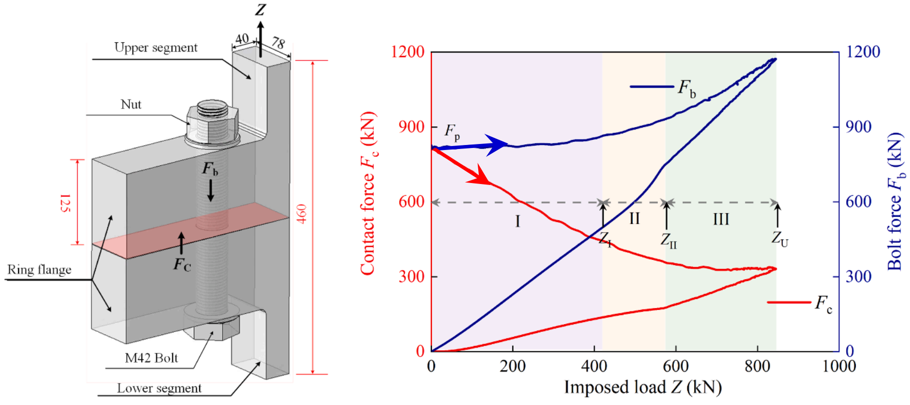

(a) RF connection (unit: mm)

(b) Evolution of bolt and contact forces

Fig. 3. Illustration of bolted ring-flange connections (RF).

limit state. This connection has been successfully certified by DNV in 2021 [30], and it is anticipated to be continually optimized and developed in a few years.

Appropriate selection of the MP-TP connection plays a significant role in the overall competitiveness of the OWFs and is essential for ensuring structural integrity. Although the investigation into the individual connection has been carried out in different aspects, there is virtually no research associated with a quantitative comparison between the above-introduced connections. Meanwhile, laboratory tests via the segment approach are generally adopted to investigate the mechanical behaviour of connection [13,31]. The constraints in hoop direction provided by the tower are not considered in the segment model. Therefore, the segment approach may not accurately reflect the continuity of the tower's connection. In pursuit of a reliable connection design, it is crucial to conduct a comparative study on the effect of the segmentation of the tower connection in deriving connection properties.

Considering that large-scale laboratory tests are expensive and difficult to perform, numerical simulation using advanced FE models can be taken as an affordable and effective method. The numerical tool is capable to provide a deeper understanding of connections than physical tests. In this paper, the FE method is adopted to simulate the mechanical behaviour of three types of connections without considering imperfections (gaps) between segments by ABAQUS. Both material inelastic and geometric nonlinearities are included in FE analysis. The developed FE models are first validated against experimental results. Subsequently, the effect of the used boundary conditions, bolt pretension force, and steel grade on tensile behaviour and fatigue performance of connections are investigated. Finally, conclusions are drawn to provide in-depth information for the practical application and further optimisation of such connections.

2. Investigated connections

This section gives a short overview of the mechanical performance of investigated connections under tensile loading in the segment model. Fig. 3 (a) illustrates the configuration of the RF connection. Two ring flange are joined by a high-strength bolt that is evenly spaced for the RF connection. Before loading, the bolt pretension F_p is applied to create a compression zone between two steel flanges. The load transfer behaviour of a typical RF connection is characterised by several stages with the imposed tensile load [19,28] (see Fig. 3 (b)).

Stage I - The increase of imposed load Z causes bending of the flanges, resulting in a nonlinear decrease of the contact force F_c. The imposed load Z is mainly resisted via the redistribution of the contact force F_c. A slight increase of the bolt force F_b appears.

Stage II - After reaching the critical value of the imposed load Z_I, a large tensile load produces the successive opening of the contacts and expeditious increment of the bolt force F_b.

Stage III - Plastic deformation, at the "macro" level, of the flange and bolt occurs in this stage after reaching Z_{II}. The bolt force F_b increase

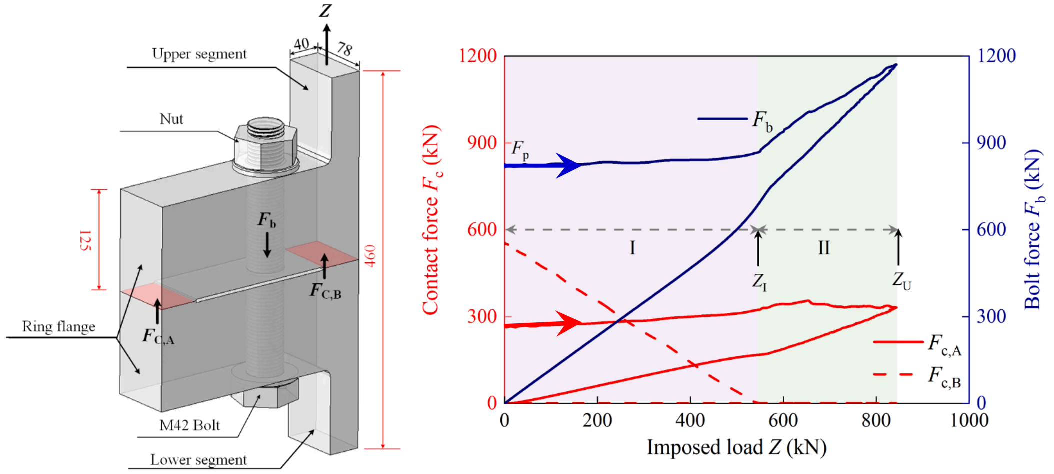

(a) RFD connections (unit: mm)

(b) Evolution of bolt and contact forces

Fig. 4. Illustration of bolted ring-flange connections with defined contacts (RFD).

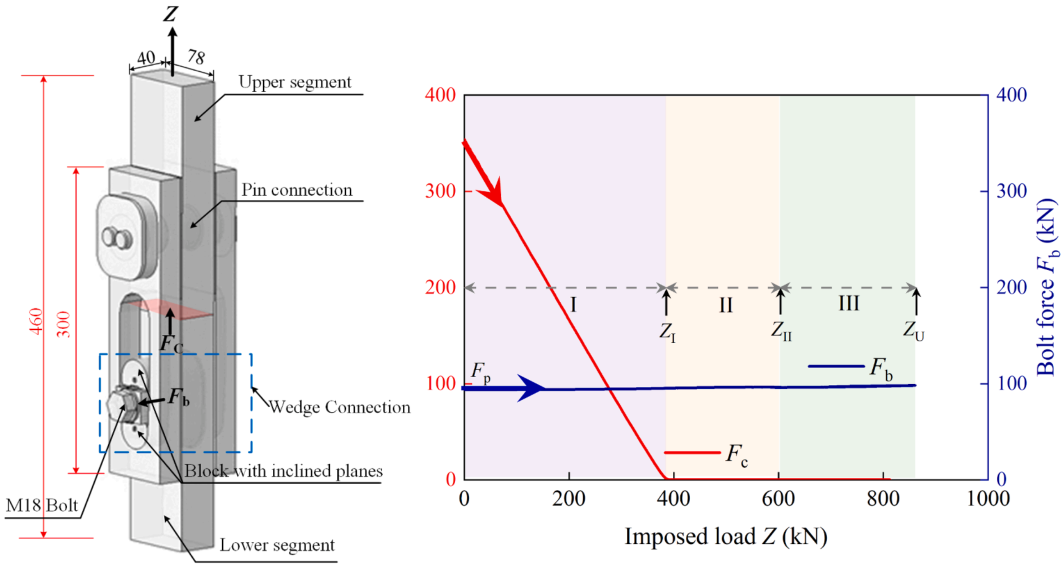

(a) C1-WC (unit: mm)

(b) Evolution of bolt and contact forces

Fig. 5. Illustration of C1 wedge connections (C1-WCs).

linearly and only the area closed to the internal edge of the flanges is in contact resulting in a roughly constant contact force F_c.

Finally, the connection achieves the ultimate tensile strength Z_U and fails in two modes: rupture of the bolts and/or rupture of the bolt combined with plastic deformation of the flanges/segments.

Different from the continuous contact surface in RF connections, in RFD connections, the pretension bolt action F_p is transmitted via two clearly defined contact surfaces. There are two deformation stages for RFD connections in tension (as shown in Fig. 4):

Stage I – The imposed load is resisted through $F_{c,B}$ (the contact area directly beneath the segment plate). The bolt force F_b and contact force $F_{c,A}$ remain unchanged until $F_{c,B}$ is fully unloaded.

Stage II – The critical load Z_I is achieved when $F_{c,B} = 0$. After that, the bolt force increases steadily until the final fracture. The ultimate capacity of the RFD connection is nearly identical to the RF connection with similar geometrical features.

Only the bolt behaviour is profoundly influenced by the distinct surfaces. Consequently, the fatigue performance of an RFD connection differs from that of an RF connection. These observations are valid for the segment model or the full ring flange without the presence of imperfections, particularly parallel gaps [32–34]. The bolt force curve increases with a steeper slope if parallel gaps are present.

Bolt pretension is horizontally applied to the C1 wedge connection. Three generations of the C1 wedge connection have been developed so far [29]. The behaviour of second-generation design with a pin connection is investigated in this paper (see Fig. 5). Two wedges immediately move towards each other with the pretension of the horizontal bolt, generating the increase in contact force F_c between the upper and lower segments. The applied tensile load is resisted by F_c at the beginning while the bolt force F_b is fairly constant throughout the loading process. The hand-calculation model was proposed by the company for designing the joint under ULS and FLS [35]. From Fig. 5 (b), the mechanical behaviour of a C1-WC is divided into three stages with the applied tensile load.

Stage I – The connection is in the elastic stage with the linearly decreased F_c. The critical load Z_I is defined at the end of the elastic stage.

Stage II – After exceeding Z_I, the connection behaves nonlinearly with increasing local plastic deformation until achieving the yield

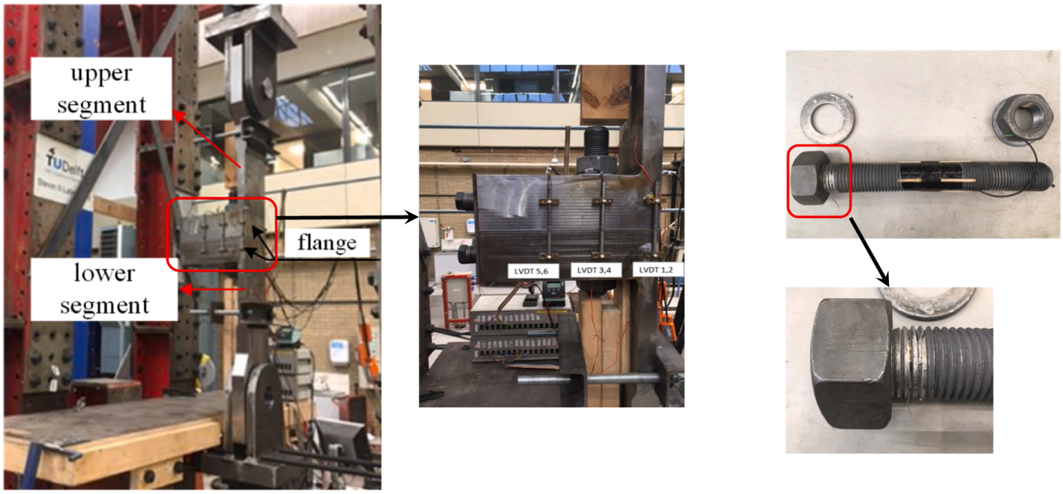

(a) Test set-up

(b) Failure mode

Fig. 6. Test set-up and failure mode for RF connections under static loads.

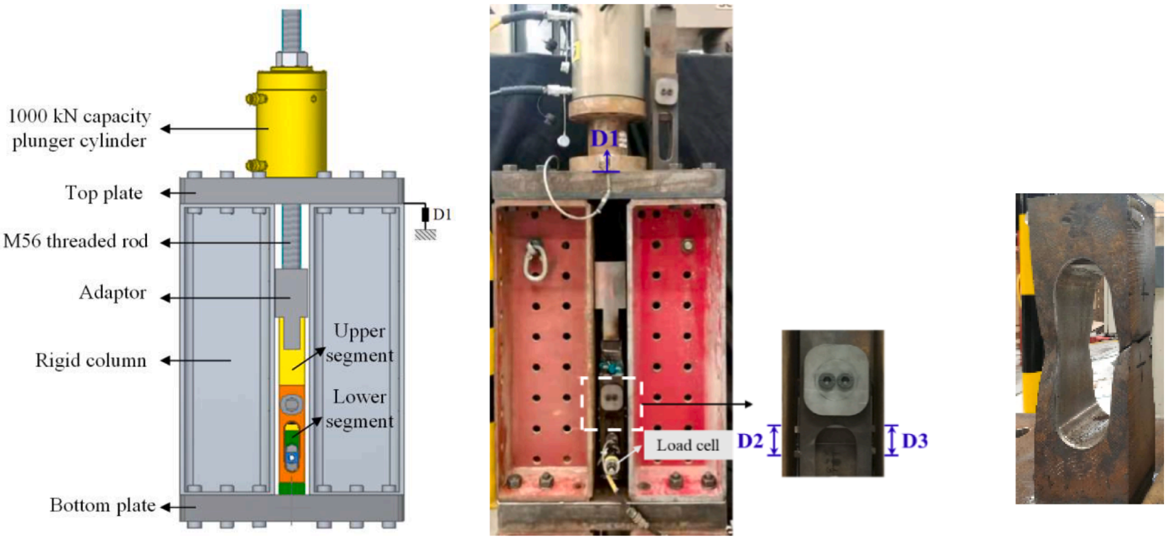

(a) Test set-up (b) Failure mode

Fig. 7. Test set-up and failure mode for C1-WCs under static loads.

strength of the lower segment (Z_{II}).

Stage III – The lower segment undergoes considerable plastic deformation successively until an apparent necking failure occurs.

3. Experimental work

The experimental program that is used to validate the FE simulation method is briefly described in this section. All the tests were performed in the Stevin II lab at TU Delft. An extensive experimental program was conducted to evaluate the static and cyclic behaviour of ring-flange connections with M56 bolts [36]. Fig. 6 shows the test set-up for RF connection under static loads. Both the top and bottom ends of the segment were supported by two hinges. After bolt preloading, the specimen was loaded to failure under displacement control. The external load, bolt forces and deformation capacity were measured. Six linear variable differential transformers (LVDTs) were installed on the sides of the flange to track the movement of the flange contact surface during loading. The bolt was instrumented with strain gauges to measure the pretension force and the following evolution of bolt force. Although various variables were analysed in this series of experiments, the experimental results of the RF connection with ISO bolt/nut assembly are used for further validation of the FE simulation method. Stripping failure of the bolt threads at the lower side of the flange was obtained from the test.

Pertaining to the C1-WC, static tests were conducted through a dedicated test set-up, as shown in Fig. 7. Different from the hinges used in the test of RF connections, the upper and lower segment were welded to rigid plates where the axial load was applied at the top plate by a hollow plunger cylinder. The applied load, bolt force and displacements in the connection were monitored during the tests. Three LVDTs (D1-D3) were mounted to measure the axial deformation of the specimens and the gap opening between the contact segments. A load cell was installed on the M18 bolt to monitor the tensile force in the bolt. M18 is employed in down-scaled experiments. The failure was governed by the net cross-section ductile failure of the lower segment. The experimental response and failure mechanism were explained in great detail by the authors [29].

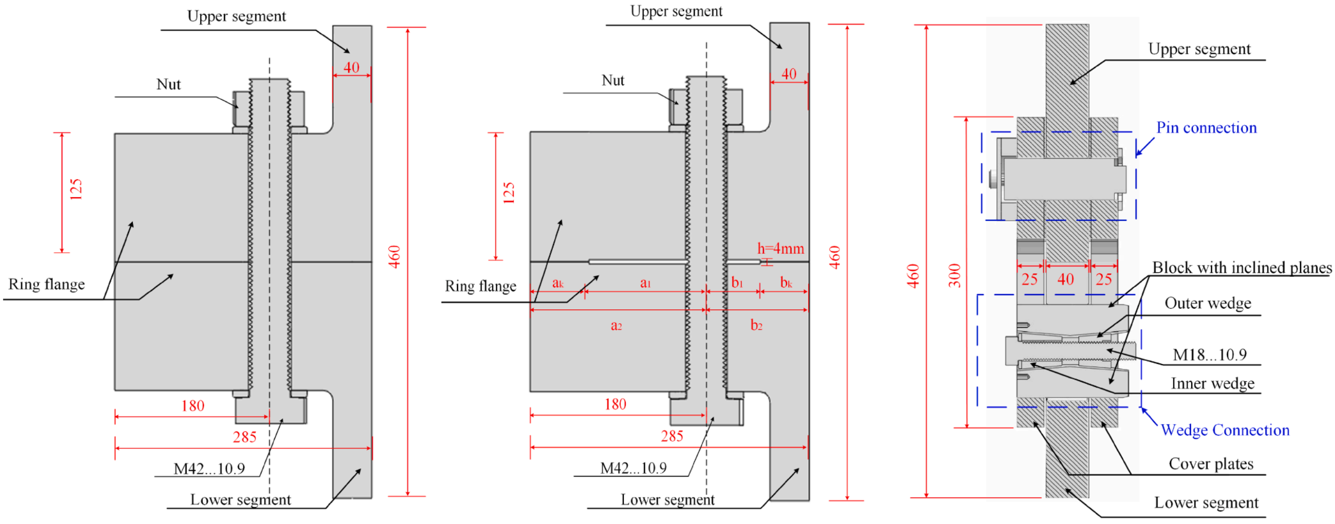

(a) RF connection (b) RFD connection (c) C1-WC

Fig. 8. Cut view of segment specimens with various connections.

Table 1
Evaluation of ultimate tensile resistance of RF/RFD connections.

Failure mode	Analytical equations	Ultimate capacity
Mode A	$F_{t,Rd} = f_{ub}A_s$	1179 kN
Mode B	$F_{U,B} = \frac{F_{t,Rd}a' + M_{pl,3}}{a' + b} = \min\left\{ \frac{F_{t,Rd}a' + \left[1 - \left(\frac{N_{ult,2}}{N_{pl,Rd,sh}}\right)^2\right]M_{pl,Rd,sh}}{a' + b}, \frac{F_{t,Rd}a' + \left[\sqrt{1 - \left(\frac{N_{ult,2}}{V_{pl,Rd,fl}}\right)^2}\right]M_{pl,Rd,fl}}{a' + b} \right\}$ [38] Note:$a' = \lambda a$ for $1.25 < a/b \leqslant 2.25$	812 kN (governing failure mode)
Mode C	$F_{U,C} = \frac{M_{pl,3} + M_{pl,Rd,fl,net}}{b} = \min\left\{ \frac{\left[1 - \left(\frac{N_{ult,3}}{N_{pl,Rd,sh}}\right)^2\right]M_{pl,Rd,sh} + M_{pl,Rd,fl,net}}{b}, \frac{\left[\sqrt{1 - \left(\frac{N_{ult,3}}{V_{pl,Rd,fl}}\right)^2}\right]M_{pl,Rd,fl} + M_{pl,Rd,fl,net}}{b} \right\}$	868 kN
Mode D	$F_{U,D} = \frac{M'_{pl,2} + \Delta M_{pl,2} + M_{pl.3}}{b'_D}$	1051 kN
Mode E	$F_{U,E} = \frac{M_{pl,2} + M_{pl,3}}{b'_E}$	2344 kN

Note: (a) The coefficient 0.9 and the partial safety factors for the ultimate tensile resistance of bolts are neglected in this study. (b) a detailed explanation can be found in [20,39] and Appendix.

4. FE modelling of connections

This study employs ABAQUS [37] to investigate the structural behaviour of the connections. All components are properly modelled to obtain accurate results from the FE analysis. The numerical simulation introduces the ductile damage material model for critical components. The associated material property parameters are chosen in accordance with the experiments. Finally, the effectiveness of the established FE models is demonstrated.

4.1. Geometry dimensions

To make a valid comparison between different connections, the geometry of connections and associated segments should be designed to have identical ultimate tensile strength. The experimental results of the C1-WC are adopted as the reference to design the RF/RFD connection. This is mainly because the design procedure for RF/RFD connection is more straightforward than the C1-WC. Hence, the developed FE model for RF/RFD connection in the comparative analysis is different from the geometrical features in the performed tests. However, the simulation method is similar so that the effectiveness of the developed FE models also can be validated using the previous test results.

It is found that the ultimate tensile resistance of the C1-WC (Z_u) is independent of the preload force applied to the bolt [29]. The segments in C1-WCs have the following characteristics: thickness and width of the segment are 40 mm and 78 mm, respectively (see Fig. 5). The ultimate capacity is calculated as $Z_u = A_{s,WC} \cdot f_u = 812$ kN, where $A_{s,WC}$ is the smallest net cross-section area of the lower segment and f_u is the measured ultimate tensile strength of S460 material [29] used in the segment of C1-WCs. Fig. 8 (c) presents the schematic geometry of the C1-WC. The M18 bolt is modelled with actual dimensions [29] measured by a digital caliper. The major diameters for the bolt and outer wedge threads are 18.18 mm and 17.90 mm, respectively. Minor diameters for the bolt and outer wedge threads are 15.20 mm and 15.48 mm,

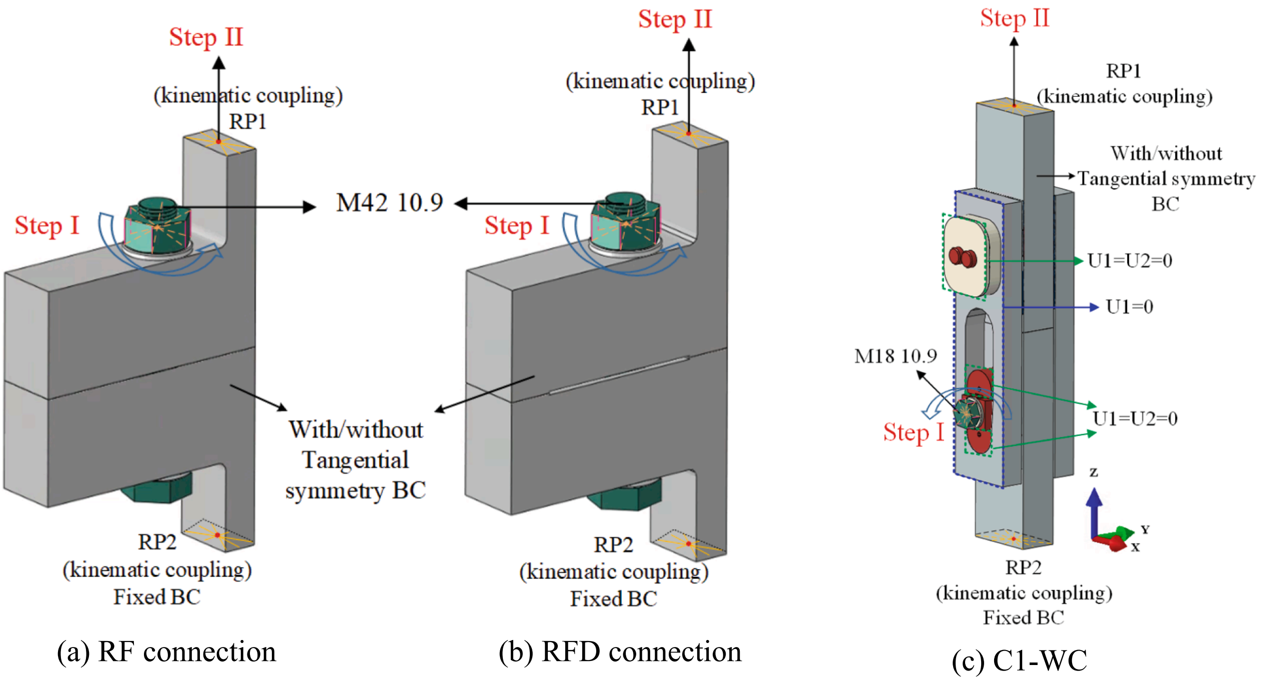

(a) RF connection (b) RFD connection (c) C1-WC

Fig. 9. Mechanical boundary conditions for various connections.

Table 2
Configuration details of FE models for RF connections.

Specimen	ρ	$F_p = \rho f_{ub} A_s$ (kN)	Rotation (rad)	Boundary condition	Steel grade	Z_I (kN)	Z_U (kN)
RF-BC1-S460	0.70	825	2.10	BC1	S460	428	845
	0.55	649	1.64			336	
	0.40	472	1.19			245	
	0.25	295	0.75			153	
RF-BC2-S460	0.70	825	2.08	BC2	S460	428	853
	0.55	649	1.63			336	
	0.40	472	1.18			245	
	0.25	295	0.74			153	
RF-BC2-S355	0.70	825	2.12	BC2	S355	428	835
RF-BC2-S690	0.70	825	2.08		S690	428	883

Note: BC1-Without tangentially symmetric boundary condition; BC2- With tangentially symmetric boundary condition.

respectively. The measured pitch is 2.5 mm which is the recommended dimension for M18 bolt according to ISO 4014 [40].

The analytical models proposed by Petersen and Seidel [10,19] are used to design the geometry of the RF/RFD connection. Five approximated failure modes are considered, and the corresponding results are shown in Table 1. The tensile resistance for failure mode A is linked to bolt failure. Failure mode B represents the failure of the bolt combined with the plastic deformation of the flange/segment. The failure of the shell and flange due to yielding is defined as failure mode C/D/E, where failure modes D/E should be used as they are more accurate and less conservative compared to using failure mode C. Table 1 shows that failure mode B controls the ULS of RF/RFD connections according to the analytical evaluation. The detailed geometry of RF and RFD connections is shown in Fig. 8 (a) and (b). A M42 bolt is utilized in these two connections. The M42 bolt is modelled in accordance with Refs. [41] and [42]. The nominal height of the bolt head and nut is 25 mm and 34 mm, respectively. The nominal bolt length is 335.5 mm. The tolerance class of threads are defined as 6g (after coating) and 6H by ISO 965–1 [43].

The parameters of the contact surface in the RFD connection are determined by the recommendations provided by Krutschinna [14]. It is obtained that the gap depth has less influence on the carrying behaviour. For the sake of manufacturing reasons, the smallest possible recess height $h/2 = 2$ mm is to be sought. The optimized value of b_k can be approximated as $b_2/2$. The parameters shown in Fig. 8 (b) are specified as: $a_k = b_k = 50$ mm, $a_1 = 130$ mm, $b_1 = 55$ mm, $a_2 = 180$ mm, $b_2 = 105$ mm.

4.2. Boundary conditions and mesh

The mechanical boundary conditions specified for these connections are shown in Fig. 9. The reference points RP1 and RP2 in the centre of the associated surfaces are kinetically coupled to the surfaces at the end, respectively. Fixed support boundary conditions are applied on RP2. The segment is uniformly arranged along a shell cylinder in a full-scale tower. The constraints caused by neighbouring shells are ignored in the conventional segment approach in laboratory conditions. To investigate the effectiveness of the conventional segment approach, various constraints are set for the free side surfaces, namely with or without tangential symmetric boundary conditions (BCs). The segment continuity corresponds to the lateral boundary condition with tangentially symmetric BC. It should be noted that the influence of tube diameter is not included here. The ideal fully constrained boundary condition is assumed in this research. While the influence of tube diameter could be considered by modelling the segment with springs in hoop direction.

Solid elements are used to model all components. The plate components are meshed using eight-node hexahedron linear solid elements with reduced integration (C3D8R). The machined components, namely the bolt, nut, threaded outer wedge, blocks and pin-bar with more complex geometry, are meshed with ten-node modified quadratic tetrahedron elements (C3D10M) to realize the free mesh. The detailed mesh for the C1-WC can be obtained from [29]. For RF/RFD connections, the global size of the solid elements in the bolt and nut is 8 mm, while in the threaded zone the element size is reduced to 3 mm. A global element size of 6 mm is used for the segments and flanges. The general contact method in ABAQUS/explicit is applied to all contact interactions [37]. The “hard” contact is defined in the normal direction to prevent penetration and tensile stress transfer across the interfaces. The tangential behaviour is modelled by a “penalty” frictional formulation which allows a relatively tiny movement between contact surfaces. The friction coefficient of 0.1 is used for all contacts in the FE models.

4.3. Computational procedure and loading

For each connection, two computation steps are carried out (see Fig. 9): bolt preloading (step I) and axial tensile loading along the Z direction (step II). The turn-of-nut method is used to apply the pretension bolt force [34]. As shown in Fig. 9, the hexagon edges of the nuts in RF/RFD connections and the bolt head in C1-WCs are kinematically connected to the reference point in their centre lines. Rotations of the reference points are applied along the axis of the bolt. The preloading

Table 3
Configuration details of FE models for RFD connections.

Specimen	ρ	$F_p = \rho f_{ub} A_s$ (kN)	Rotation (rad)	Boundary condition	Steel grade	Z_I (kN)	Z_U (kN)
RFD-BC1-S460	0.70	825	2.35	BC1	S460	543	843
	0.55	649	1.83			427	
	0.40	472	1.33			310	
	0.25	295	0.84			194	
RFD-BC2-S460	0.70	825	2.29	BC2	S460	543	853
	0.55	649	1.79			427	
	0.40	472	1.30			310	
	0.25	295	0.82			194	
RFD-BC2-S355	0.55	649	1.79	BC2	S355	427	835
RFD-BC2-S690	0.55	649	1.80		S690	427	882

Note: BC1-Without tangentially symmetric boundary condition; BC2- With tangentially symmetric boundary condition.

Table 4
Configuration details of FE models for C1-WCs.

Specimen	ρ	$F_p = \rho f_{ub} A_s$ (kN)	Rotation (rad)	Boundary condition	Steel grade	Z_I (kN)	Z_U (kN)
WC-BC1-S460	0.70	141	51.60	BC1	S460	762	817
	0.55	111	38.95			625	
	0.40	80	29.88			467	
	0.25	50	21.58			303	
WC-BC2-S460	0.70	141	49.59	BC2	S460	752	826
	0.55	111	38.05			618	
	0.40	80	29.19			450	
	0.25	50	21.27			294	
WC-BC2-S355	0.40	80	29.19	BC2	S355	221	682
WC-BC2-S690	0.40	80	29.19		S690	450	1032

Note: BC1-Without tangentially symmetric boundary condition; BC2- With tangentially symmetric boundary condition.

Table 5
Material properties adopted in FE models.

Components	Color	Material	E_0 (MPa)	f_y (MPa)	f_u (MPa)	ε_u	A	W	α	β
Washer/pin connection	White	Elastic	2.10e5	–	–	–	–	–	–	–
Fastener assembly	Red	34CrNiMo6	2.10e5	620	800	–	0.15	–	–	–
Bolt/nut	Green	10.9	2.10e5	957	1062	0.050	0.10	0	2	1.5
Plate	Grey	S355	2.10e5	375	517	0.175	0.32	0.1	1.8	1.5
		S460	2.10e5	485	620	0.125	0.23	0	1.4	
		S690	2.05e5	746	785	0.061	0.15	−0.4	1.3	

Note: E_0 – Young's modulus; f_y and f_u is yield and ultimate tensile strength, respectively; ε_u - the strain corresponding to ultimate tensile strength; A - the ultimate elongation; W – weighting factor in full-range true stress–strain constitutive material model; α and β are two material-dependent parameters in Rice-Tracy fracture criterion.

forces in the bolt are obtained by measuring the contact pressure force at the inner washer surface. EN 1090–2 [44] states that the design bolt pretension force $F_{p,C}$ should be calculated using $F_{p,C} = \rho \cdot f_{ub} \cdot A_s$ ($\rho = 0.70$), where f_{ub} is the ultimate tensile strength of bolts; A_s is the tensile section area of the bolt. The partial safety factor is not considered in this paper. Four different values of the preload coefficient ρ ranging from 0.25 to 0.70 are selected to investigate the effects of levels of F_p. Hence, various rotation angles are adopted to achieve different F_p, as shown in Table 2, Table 3, and Table 4. After preloading, axial tensile displacement along Z direction is implemented to RP1 at the top of the segment.

An explicit solver is used to overcome the problem of convergence difficulties and enhance computational efficiency. After trial computations, a semi-automatic mass scaling option is used to shorten the computation time and guarantee the quasi-static analysis. The difference in the applied rotation between RF/RFD connections and C1-WCs is obvious. In contrast to applying pretension force in the bolt to clamp the flanges in RF/RFD connections, the horizontal bolt in the C1-WCs causes the movement of two wedges. Under applying the same rotation, the resulting bolt extension in RF/RFD connections is much larger than that in the C1-WCs. It is reported that the bolt head rotation of 2.8 rad only generates a 10 kN increment in F_p in C1-WCs [29]. Consequently, the target time increment and period are different during the simulation for these connections. The target time increment for RF/RFD connections is set to be 0.5×10^{-6} s. The associated periods adopted for preloading and loading to failure steps are 0.1 s and 0.05 s, respectively. For the C1-WC, the time increment is set as 1.0×10^{-6} s. The periods for preloading and tensile loading are 2.5 s and 0.25 s, respectively.

4.4. Material models

Table 5 provides a list of the mechanical characteristics of the materials utilized in the FE model. Four kinds of material are introduced for major components in FE models, and they are displayed by colours in Fig. 9. Three steel grades (S355/S460/S690) is specified for plate component to quantify the effect of steel strength on the mechanical performance of connections. The washer and pin connection parts are modelled as an elastic material, while elastic–plastic material is used to model other components. As insignificant plastic deformation occurs in machined parts in C1-WCs, the material behaviour of fastener assembly is represented by an idealized trilinear elastic–plastic hardening model, as shown in Fig. 10. Nominal material properties are adopted according to EN 10025–6 [45]. Engineering stress–strain curves are transformed into true stress–strain curves as input data in the ABAQUS plasticity model [46].

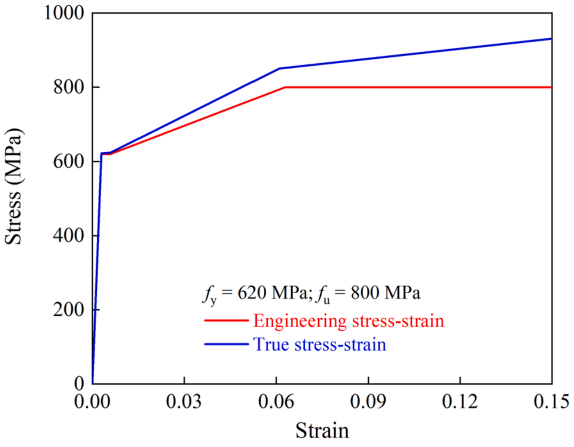

Fig. 10. Stress–strain curves for 34CrNiMo6 material.

The full-range stress–strain constitutive model and ductile damage model are used for plate components and bolts. The post-necking behaviour of metal material can be successfully described by a combined linear and power law stress–strain law [46–48]. The only unknown variable, namely weighting factor W, is calibrated using the measured material property. To accurately simulate the failure mode of connections, a ductile damage model based on Rice-Tracey (RT) function is employed in this study [49,50]. Two material-dependent parameters α and β are calibrated by matching the engineering stress–strain curves obtained from test results [29,51–53], see Fig. 11. It should be noted that the material property of the bolt is obtained based

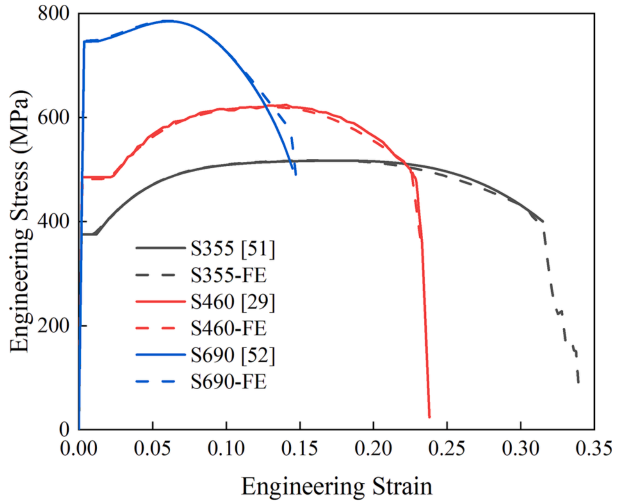

Fig. 11. Comparison between experimental and numerical engineering stress–strain curves.

on the assumption of a parabolic shape of the engineering stress–strain curve [34]. The curves can be drawn with measured yield and ultimate tensile strength and the ultimate elongation $A = 10$ % according to ISO 898–1 [54]. Fig. 12 shows the calibrated full-range stress–strain curves for materials specified for plate components and bolts.

4.5. Validation of FE method

The developed FE method for C1-WCs has been demonstrated in [29]. As mentioned before, the FE simulation method for RF/RFD connection is validated by the test results described in section 2. In the test, after applying 5 cyclic loads via force control, the specimen was loaded to final failure via displacement control. An FE model with identical geometry and boundary conditions to the test is established. Uniaxial tensile load applied in the cross-section of the upper segment is used in FE simulation for simplification. Comparisons are made between numerical and experimental ultimate load capacity, bolt force evolution, and local deformation, as illustrated in Fig. 13. After the bolt exceeds its yield strength (F_b greater than 1942 kN), the actual experimental bolt force was not available from the used strain gauges. This is because the strain is not proportional to the bolt force outside the elastic region. The maximum bolt force $F_{b,max\text{-}test}$ was calculated according to the established simple analytical model: $F_{b,max-test} \times a = Z_{max-test} \times (a + e)$. a is the distance from the bolt axis to the flange edge, and e is the distance from the bolt axis to the shell mid plane at final fracture. The ultimate capacity of the specimen ($Z_{max\text{-}test}$) and the bolt ($F_{b,max\text{-}test}$) are also shown in Fig. 13 (a). It is found that the FE model can accurately predict the strength of the specimen and the bolt. As plotted in Fig. 13 (b)-(d), the simulated gap curves provide relatively good agreements with the envelope of the test results. The difference shown in Fig. 13 (b) is because LVDT1 and LVDT2 went out of range before the ultimate tensile strength during the test. Both experimental and numerical results show the bolt failure mode. Therefore, it is concluded that the FE simulation method for the RF connection realistically predicts the mechanical behaviour of this connection.

5. Parametric studies on tensile behaviour

In this section, the influence of important parameters on the behaviour of connections under static loading is assessed based on the validated FE method. The parameters include the lateral boundary condition on the sides of the segment/flange in hoop direction (BC1/

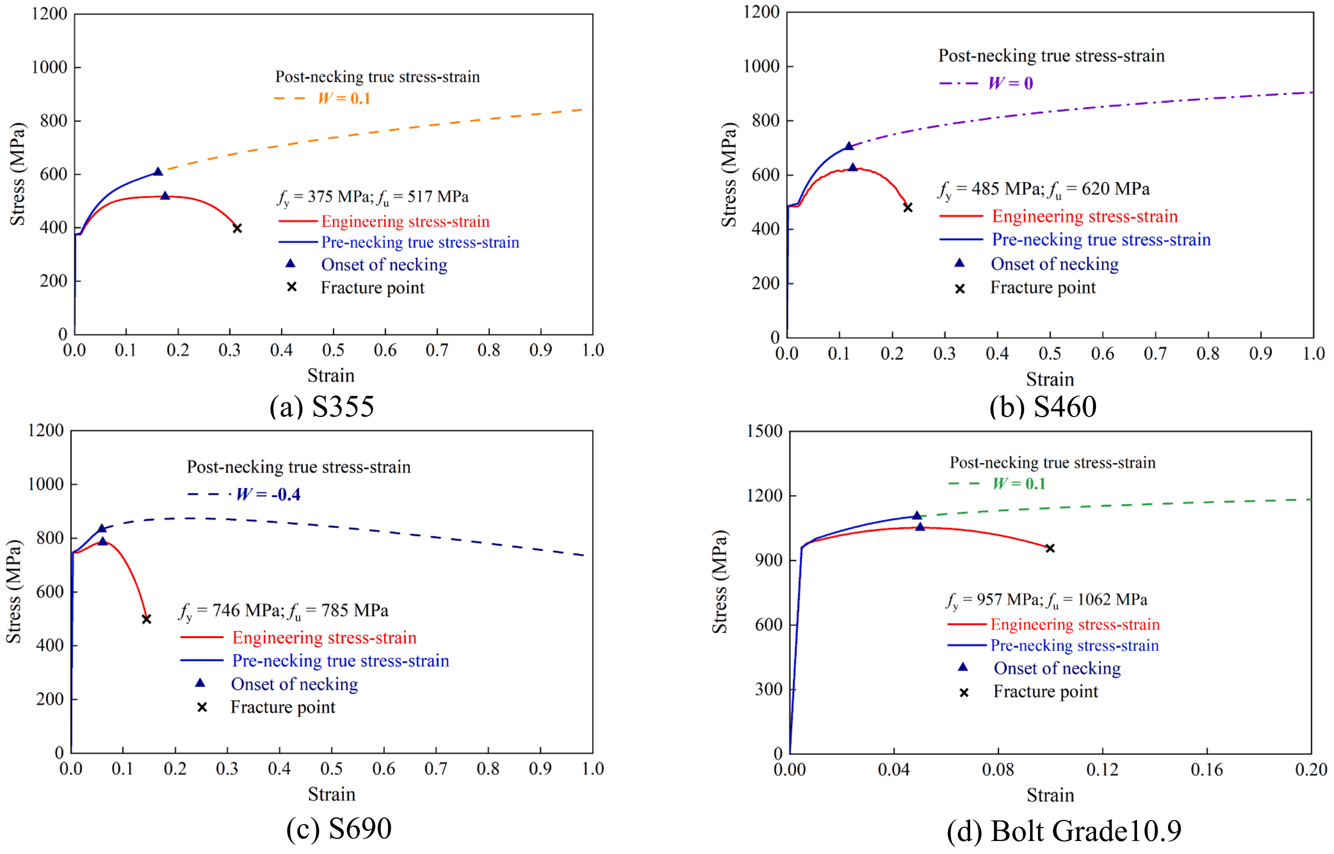

(a) S355 (b) S460

(c) S690 (d) Bolt Grade10.9

Fig. 12. Stress–strain curves of the critical parts in FE models.

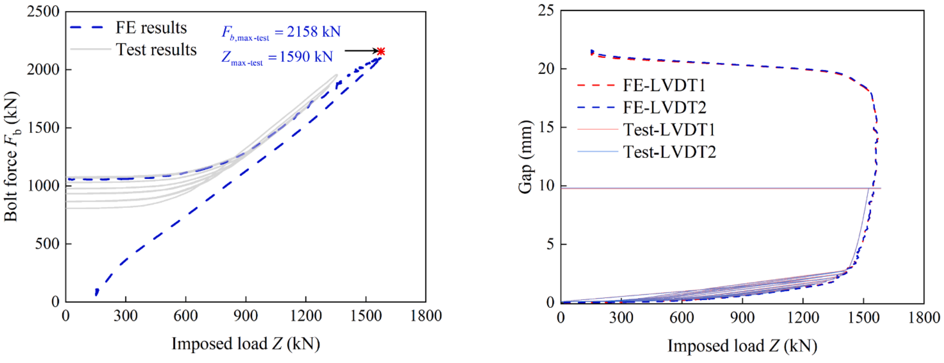

(a) Bolt force F_b

(b) Gap at LVDT1/2

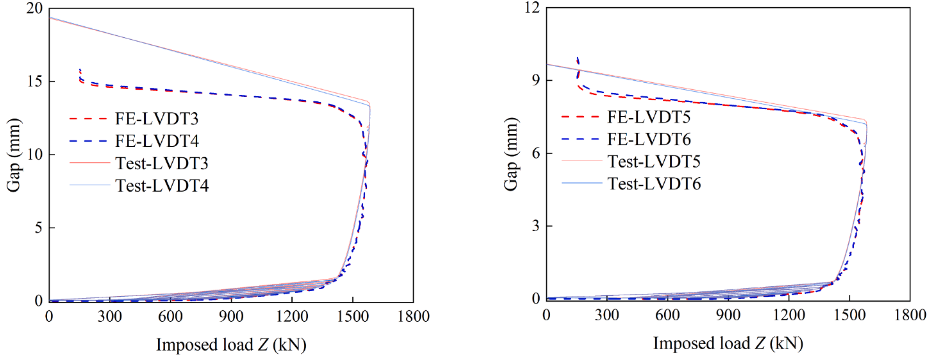

(c) Gap at LVDT3/4

(d) Gap at LVDT5/6

Fig. 13. Comparison between FE and test results of RF connections.

BC2), preload coefficient ρ (0.70, 0.55, 0.40, and 0.25), and the steel strength (S355, S460, and S690).

5.1. Effect of BC1/BC2

The FE models with the preload coefficient $\rho = 0.7$ are taken as the benchmark to analyse the effects of lateral boundary conditions. The detailed results are summarized in Table 2 and Table 3. Fig. 14 represents the effect of BC1/BC2 on the behaviour of RF and RFD connections, namely specimens RF-BC1/BC2-S460 and RFD-BC1/BC2-S460. An insignificant variation is found between RF-BC1-S460 and RF-BC2-S460 in terms of load–displacement curves, evolution curves of bolt force, and gap between segments in the back view (see Fig. 14 (a), (c), and (e)). A similar observation is found for RFD-BC1-S460 and RFD-BC2-S460. These imply that the lateral boundary conditions have little influence on the tensile performance of RF and RFD connections. Although the deformation of the shell and flange is constrained with BC2, the bolt is the critical component of RF/RFD connections. The circumferential stress generated under BC2 has negligible influence on the static tensile behaviour of RF/RFD connections. It is reasonable to use the segment approach to represent their static performance without considering imperfections. The bolt force evolution calculated using proposed analytical models is included in Fig. 14 (c) and (d) to strengthen the reliability of the FE models. It is found the Schmidt/Neuper estimation is conservative as reported in [13], which is accepted to contain the detrimental influence of imperfections. The development of F_b obtained from analytical models for RFD connections agrees well with the FE results.

Fig. 15 illustrates the comparison between WC-BC1-S460 and WC-BC2-S460. A noticeable contrast begins at the yield plateau in load–displacement curves and continues until the approximate peak load (see Fig. 15 (a) and Table 4). The evolution curves of bolt force exhibit almost identical behaviour with BC1 and BC2, see Fig. 15 (b). This is attributed to the fact that the bolt contributes less to directly resist the tensile load. The major function of the horizontal bolt is to provide contact pressure between segments, and not as in RF/RFD connections to contribute directly to the tensile force transfer. It is reported that the lower block in the C1-WC is subjected to bending as it spans two cover plates and the lower segment [16]. After reaching the ultimate capacity, the obvious deformation in the lower segment results in increased bending in the lower block and the bolt. The axial force distribution in the middle cross-section of the bolt is displayed in Fig. 15 (b). With the significantly increased deformation in the lower segment, the contact between the lower wedge connection and the lower segment is lost followed by the suddenly decreased bolt force. Meanwhile, the contact force is dominantly distributed in the middle of the segment no matter under which boundary conditions. Hence, the lateral boundary condition has a negligible effect on the gap between the segments in the back view (see Fig. 15 (c)). A control point is located at the transition region in the lower segment instead of the bolt from FE results. The maximum principal stress $\sigma_{\text{pri,max}}$ at this point until the maximum strength is extracted as shown in Fig. 15 (d). It is found that $\sigma_{\text{pri,max}}$ increases linearly until reaching the yield limit strength f_y. With increasing imposed load, $\sigma_{\text{pri,max}}$ of WC-BC1-S460 exhibits a faster increase rate with a smaller initial value compared to that of WC-BC2-S460.

To better reflect the effect of BC1/BC2, the deformation and stress response of the lower segment under the imposed load of 240 kN is shown in Fig. 16 as an example. The stress distribution at a certain cross-section of the hole is also displayed in Fig. 16. The deformation along X direction is magnified with a factor of 50. It is seen that the distribution of $\sigma_{\text{pri,max}}$ is heavily influenced by BC1 and BC2. Moreover, the distribution of $\sigma_{\text{pri,max}}$ along the centre line of half oval hole is represented in Fig. 17. The negative max. principal stress occurring between $0^\circ - 25^\circ$ is attributed to the compression force between the upper block and the lower segment at this region. The diagrams show that BC1 causes a more uniform distribution of stress response in the C1-WC. This could explain why the value of $\sigma_{\text{pri,max}}$ of WC-BC1-S460 at the control point (see Fig. 15 (d)) is smaller than the WC-BC2-S460 before reaching yield strength.

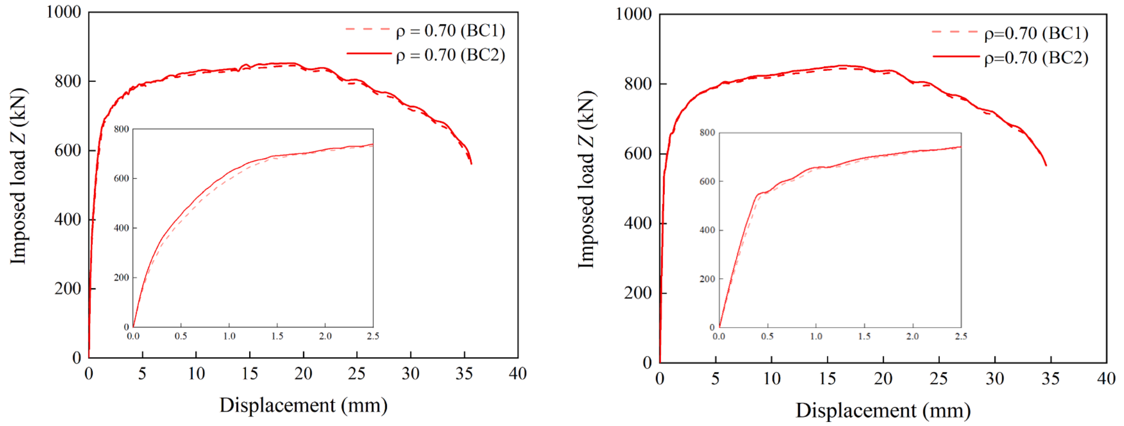

(a) RF-BC1/BC2-S460

(b) RFD-BC1/BC2-S460

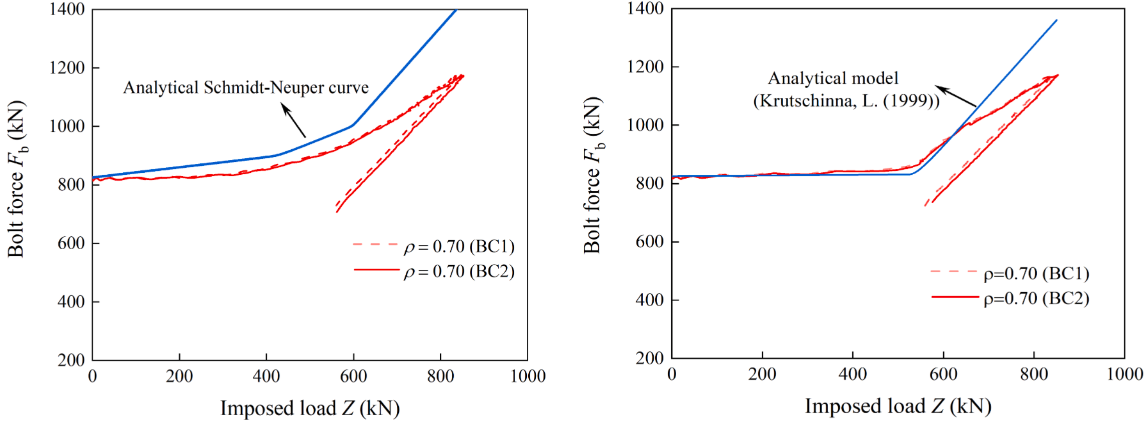

(c) RF-BC1/BC2-S460

(d) RFD-BC1/BC2-S460

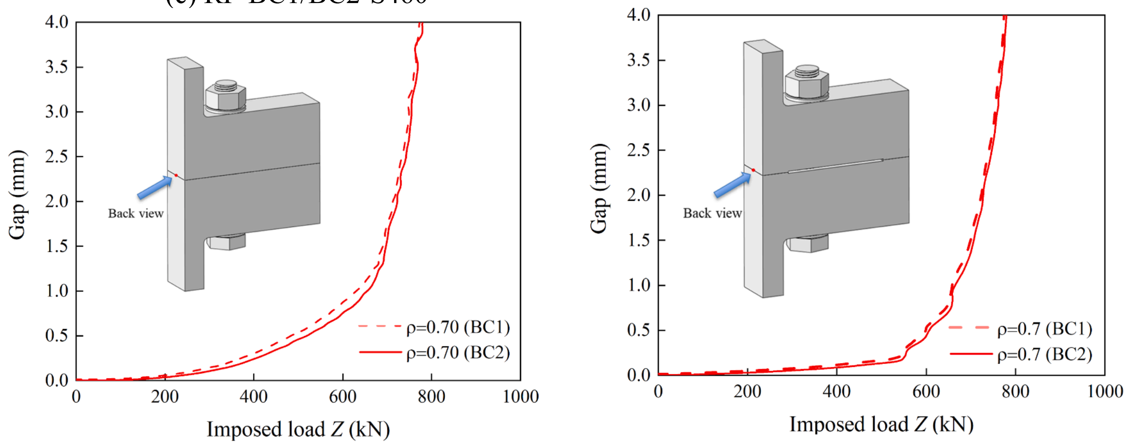

(e) RF-BC1/BC2-S460

(f) RFD-BC1/BC2-S460

Fig. 14. Comparison of RF and RFD connections: (a) and (b) load–displacement curves, (c) and (d) bolt force evolution curves, and (e) and (f) gap.

Analysing the range of maximum principal stress $\Delta\sigma_{\mathrm{pri,max}}$ and the stress concentration factor (SCF) k_f is crucial to identify the most vulnerable regions under fatigue in the lower segment in C1-WCs. To eliminate the influence of the initial stress introduced by various pretension levels (see Table 4), SCF is defined as the ratio of $\Delta\sigma_{\mathrm{pri,max}}$ to the nominal stress for this connection. The grey shadow area marked in Fig. 17 is located between the angle 25°-80°. Fig. 18 displays the response of $\Delta\sigma_{\mathrm{pri,max}}$ and k_f in these localized regions, where $Z = 0$ kN is selected as the reference. As shown in Fig. 18, the position of the peak $\Delta\sigma_{\mathrm{pri,max}}$ differs under BC1 and BC2. The $k_{f,\max}$ corresponding to peak $\Delta\sigma_{\mathrm{pri,max}}$ is obtained as 1.50 and 1.41 for WC-BC1-S460 and WC-BC2-S460, respectively. The $\Delta\sigma_{\mathrm{pri,max}}$ and k_f under BC1 are higher than those under BC2. This is because the circumferential continuity (hoop stresses) causes increasing triaxiality followed by the larger SCF. It implies that the stress response in the lower segment of C1-WCs is greatly influenced by "circumferential" boundary conditions.

5.2. Effect of pretension level (coefficient ρ)

The effect of pretension level on the behaviour of RF, RFD, and C1-WC is shown in Fig. 19 and Fig. 20. The results of connections with BC2 are selected for comparison. The initial stiffness of these connections is degraded with reduced ρ (see Fig. 19 (a) and (b), Fig. 20 (a)). For RF and RFD connections with insufficient pretension force, the obvious rise of the bolt force F_b and gap appears earlier together with the lower critical value Z_I (see Table 2 and Table 3). As shown in Table 4 and

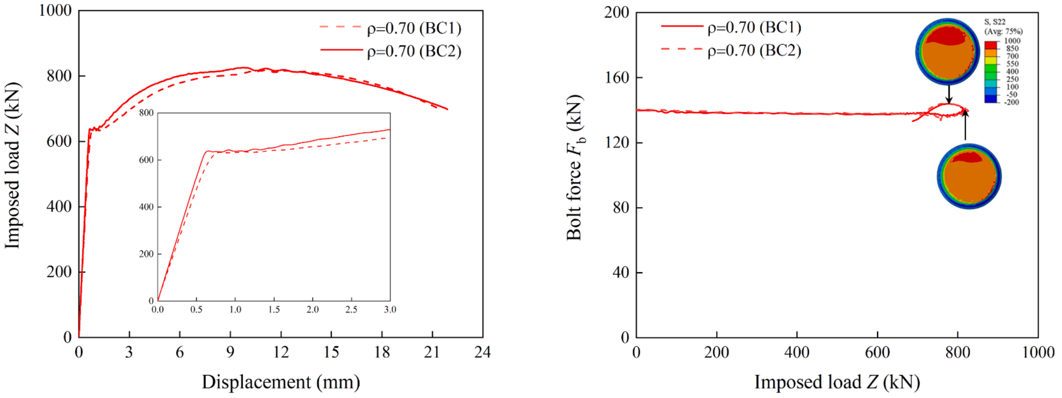

(a) Load-displacement curves

(b) Evolution curves of bolt force

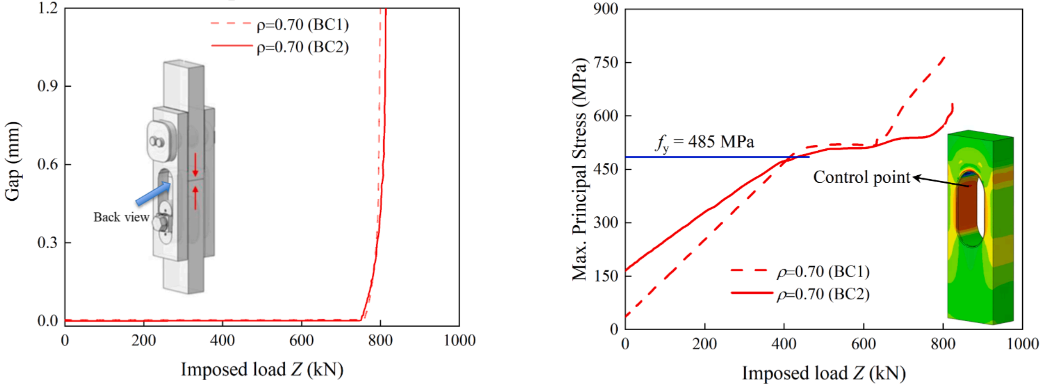

(c) Gap

(d) Maximum principal stress

Fig. 15. Comparison between WC-BC1/BC2-S460.

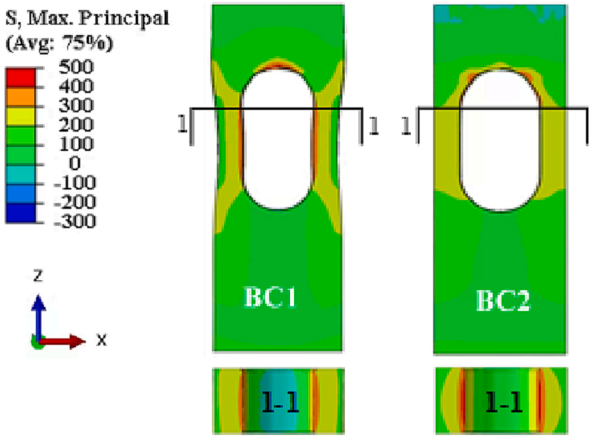

Fig. 16. Deformation and stress response of WC-BC1/BC2-S460 under Z = 240 kN.

Fig. 20 (b), Z_I corresponding to the abruptly appearing gap between segments in C1-WCs also decreases with reduced ρ. It should be noted that the ultimate capacity Z_U for all types of connections is not related to the pretension level.

Fig. 21 compares the response of maximum principal stress at the control point of C1-WCs under various boundary conditions and preload coefficient ρ. It is interesting to find that the stress response of WC-BC1-S460 is approximately consistent under various ρ, see Fig. 21 (a) and (b). However, larger ρ in WC-BC2-S460 generates a higher initial value of $\sigma_{\mathrm{pri,max}}$ after preloading and lower SCF $k_{f,\max}$ before yielding strength. The lowest $\Delta\sigma_{\mathrm{pri,max}}$ and $k_{f,\max}$ of WC-BC2-S460 with ρ = 0.70 demonstrate the benefits of sufficient pretension level in C1-WCs. These results also necessitate the importance of investigating the lateral boundary conditions.

5.3. *Effect of steel strength*

To quantify the influence of various steel grades, the mechanical behaviour of RF and RFD connections with identical Z_I and boundary conditions are compared in this section. According to the analytical models, Z_I of RF connections with $\rho = 0.7$ is calculated as 428 kN which is equal to that of RFD connections with $\rho = 0.55$. Fig. 22 displays the comparison analysis between RF and RFD connections made of various steel grades. The governing failure mechanism is the plastic hinge in the shell/flange and the failure of the bolt. The ultimate resistance is increased by using higher steel grade for shell and flanges (Fig. 22 (a) and (b)). As presented in Fig. 22, the curves separate after reaching the imposed load of 720 kN both for RF and RFD connections. It is found that the nominal bolt stress exceeds the yield strength of bolts of 957 MPa under 720 kN. This implies that the imposed load is resisted by the introduced contact force between flanges, bolts, and the segments/flanges sequentially. Before bolts yield, the major function of the shell and flange is to transfer the external load. The steel strength has no influence on the initial stage of the bolt force development and gap behaviour for RF/RFD connection. This is verified by the FE results as displayed in Fig. 22 (c)-(f).

Fig. 23 shows the comparison between WC-BC2-S355, WC-BC2-S460, and WC-BC2-S690. The design value of critical load Z_I is 450 kN. The segments in C1-WCs are the dominant part to resist the imposed load, instead of the bolt in RF and RFD connections. Therefore, these three specimens behave differently in terms of the load–displacement curves, gap opening, and stress response. It is seen that the gap of WC-BC2-S355 develops much earlier than the other two specimens (Fig. 23 (b)). Under the designed critical load Z_I, the maximum principal

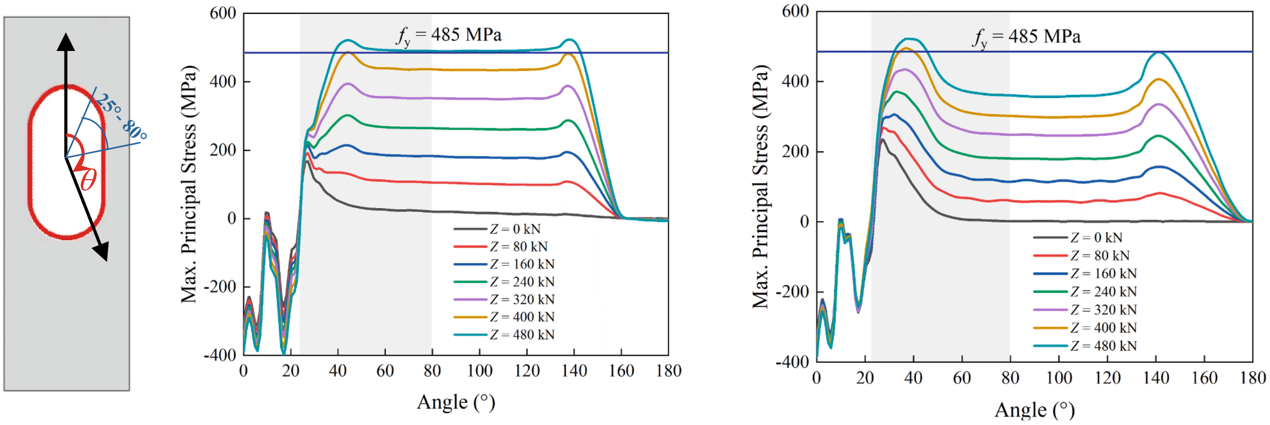

(a) WC-BC1-S460 (b) WC-BC2-S460

Fig. 17. Distribution of max principal stress of C1-WCs under BC1/BC2.

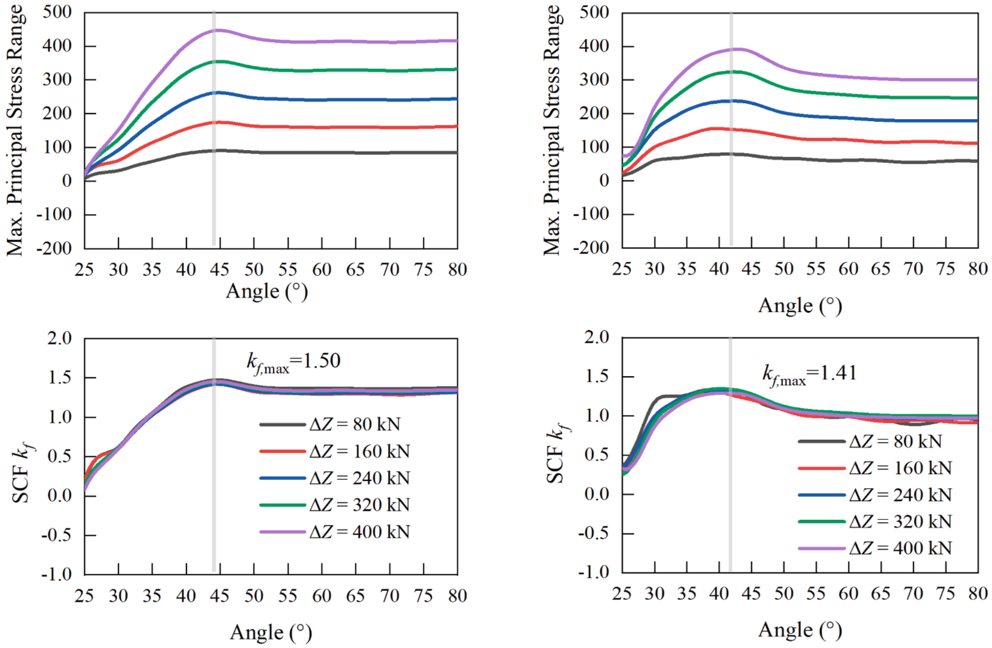

(a) WC-BC1-S460 (b) WC-BC2-S460

Fig. 18. Comparison of maximum principal stress range and SCF for WC-BC1/BC2-S460.

stress of WC-BC2-S355 is around 400 MPa representing the appearance of developed plastic deformation, as shown in Fig. 23 (c). It is required that the connections are in the elastic stage, e.g. below the critical load Z_I load. The steel grade lower than S355 is not enough to satisfy the requirement. Therefore, it is suggested that the yield strength of steel grade in C1-WCs should be larger than $Z_I/A_{s,WC}$ for design, where $A_{s,WC}$ is the smallest net cross-section area of the lower segment [55].

6. Parametric studies on fatigue performance

Typically, the fatigue performance of RF/RFD connections is dependent on the bolt force response [56,57]. Fig. 24 displays the distribution of stresses S33 along the bolt length of RF-BC2-S460. The stress range Δσ is calculated as $\Delta\sigma = \Delta F_b/A_s + 2\cdot\Delta M\cdot d_{bolt}/I_{bolt}$, where A_s is the tensile stress area of the bolt, d_{bolt} is the effective diameter of the bolt, and I_{bolt} is the moment of inertia of the bolt. The axial force F_b and bending moment M are extracted using a free body cut with 100 slicing along the bolt length. A smooth curve is then produced using a cubic smoothing spline to mitigate the effect of scattering. The critical point locates in the first engaged thread, which is consistent with the previous study [58]. The discussion in section 5 shows the effect of BC1/BC2 and steel strength on the bolt behaviour for RF/RFD connections is negligible before reaching Z_I. On the contrary, insufficient pretension force raises the range of bolt force response, hence reducing the fatigue resistance of connections. Moreover, recent studies have reported that the fatigue performance of these connections cannot be effectively evaluated by the segment approach without considering the flange imperfections [59,60]. In RF/RFD connections, flange imperfections are “almost” unavoidable due to fabrication and execution, as the flange surfaces are typically uneven and with unparallel gaps in real situations [61]. A log-normal distribution of the size of the imperfections has been reported by Buchholz et al. [62] based on more than 1900 flatness measurements of OWF projects. Flange imperfections have a significant effect on the bolt response and the fatigue performance of the RF/RFD connections. In

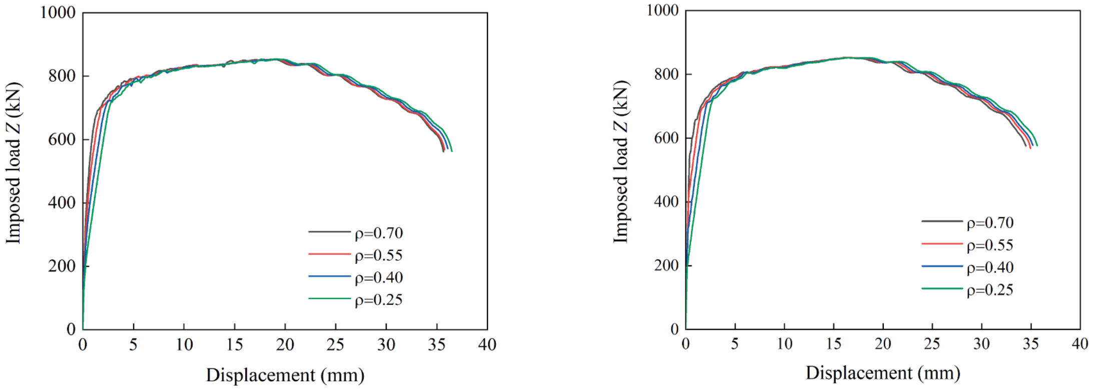

(a) RF-BC2-S460

(b) RFD-BC2-S460

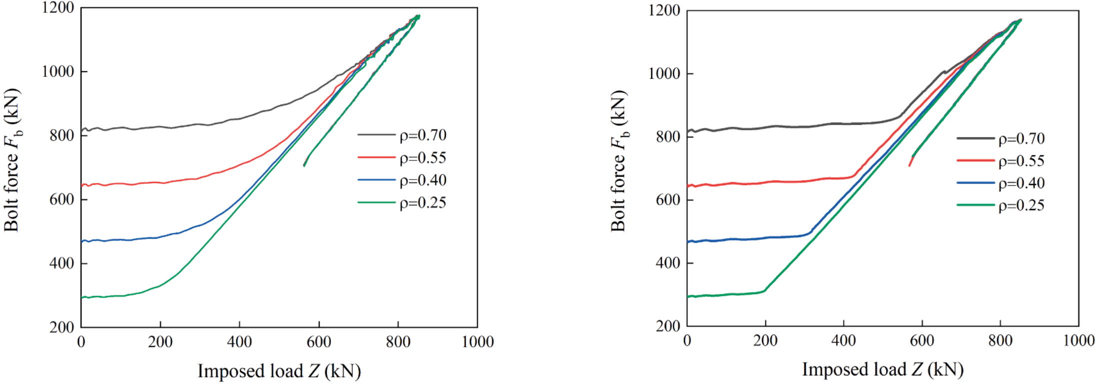

(c) RF-BC2-S460

(d) RFD-BC2-S460

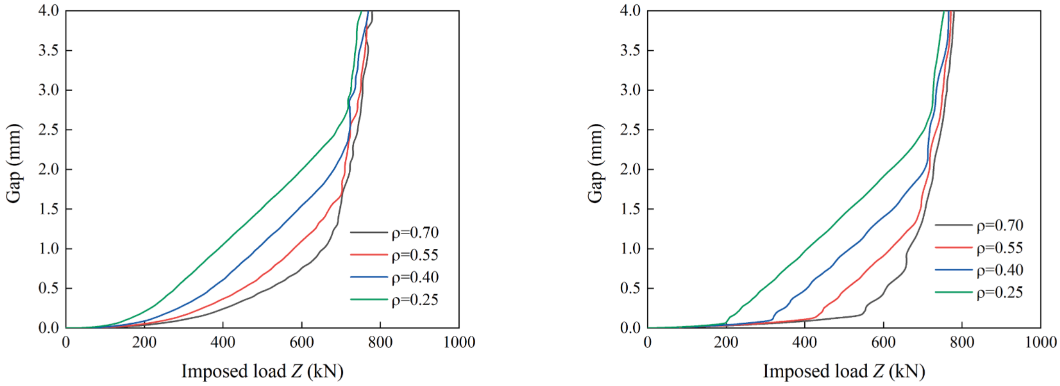

(d) RF-BC2-S460

(e) RFD-BC2-S460

Fig. 19. Comparison of RF/RFD connections under various preload coefficient: (a) and (b) load–displacement curves, (c) and (d) bolt force evolution curves, and (e) and (f) gap.

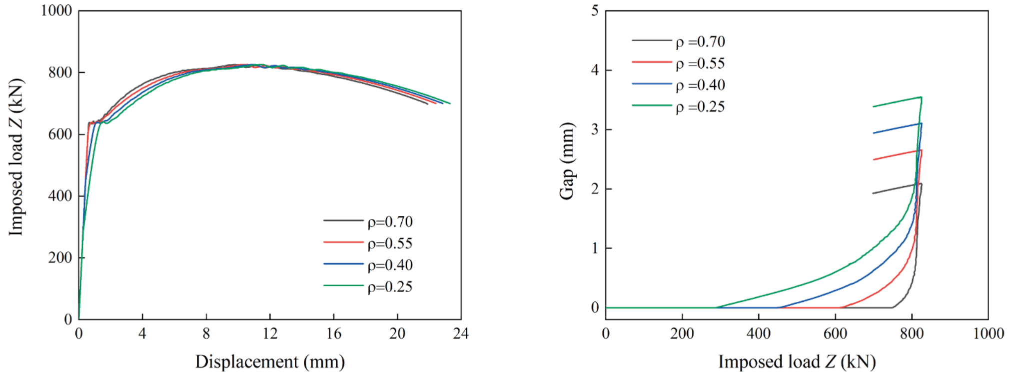

(a) Load-displacement curves

(b) Gap

Fig. 20. Comparison of WC-BC2-S460 under various preload coefficient.

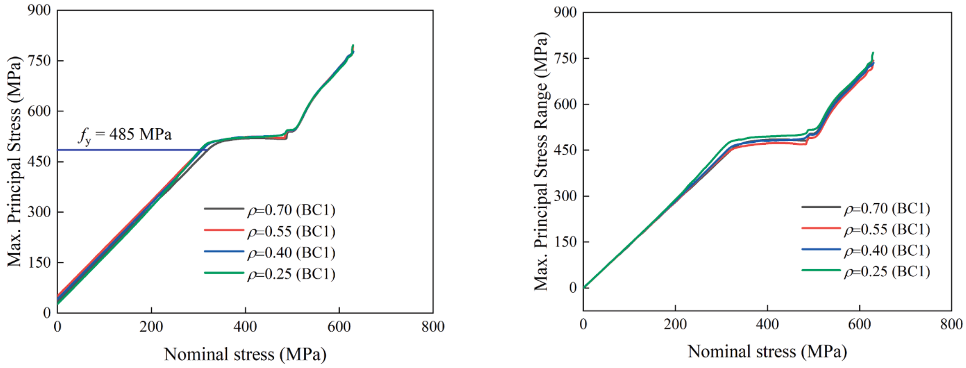

(a) $\sigma_{\mathrm{pri,max}}$ of WC-BC1-S460 (b) $\Delta\sigma_{\mathrm{pri,max}}$ of WC-BC1-S460

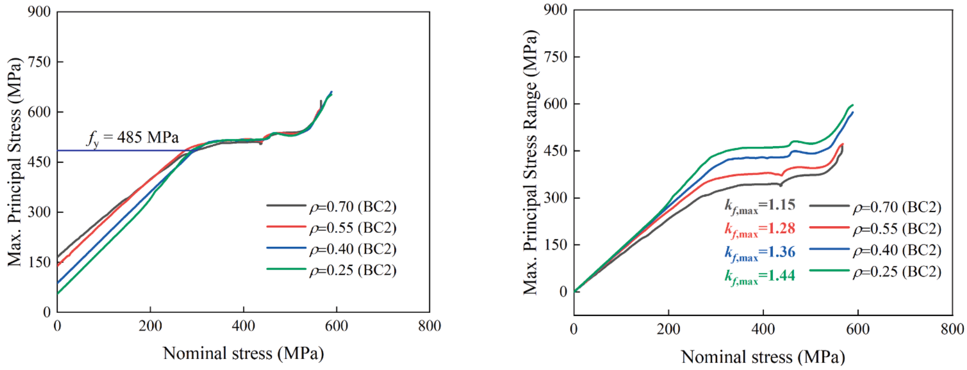

(c) $\sigma_{\mathrm{pri,max}}$ of WC-BC2-S460 (d) $\Delta\sigma_{\mathrm{pri,max}}$ of WC-BC2-S460

Fig. 21. Response of maximum principal stress of C1-WCs under various BC and ρ.

short, the segment approach is not suitable for the fatigue design prediction of RF/RFD connections, and therefore the fatigue assessment using the segment approach is not discussed in the paper.

Referring to the C1-WC, a log–log relation between stress range and fatigue life is obtained as $\log_{10}(N) = 12.282–3 \times \log_{10}(\Delta\sigma)$ with 75 % confidence level and 95 % probability of survival based on the scaled segment fatigue tests. The fatigue life S—N curves employed to evaluate the fatigue performance of the connections are shown in Fig. 25. The detail category $\Delta\sigma_C$ is predicted as 98 according to the definition in [56]. It should be noted a more comprehensive FLS assessment is required to confirm the detail category for C1-WC. The analyses in section 5 show that the stress response of C1-WCs is significantly influenced by BC1/BC2, pretension force level, and steel strength. Therefore, an evaluation of the fatigue life of C1-WCs is presented. The range of maximum principal stress $\Delta\sigma_{\mathrm{pri,max}}$ is used for calculating fatigue resistance. In that case, the detail category incorporated with the stress concentration factor k_f should be used. k_f varies with different pretension levels under BC2. For simplification, $k_f = 1.5$ is used and the detail category FAT 98 is substituted by FAT 147 when using $\Delta\sigma_{\mathrm{pri,max}}$ as the stress range.

Results of the stress range in C1-WCs under five nominal stress ranges ($\Delta\sigma_{\mathrm{seg}}$) applied to the top of the upper segment are shown in Table 6. It is noticed that the $\Delta\sigma_{\mathrm{pri,max}}$ of C1 WCs with BC2 is smaller than that with BC1 under the identical nominal stress range. The calculated stress ranges are then used to compute the related fatigue life. Results including the ratio between the fatigue life under BC1 and BC2 ($N_{\mathrm{BC1}}/N_{\mathrm{BC2}}$) are displayed in Table 7. The results of the fatigue life evaluation are more vividly presented in Fig. 26. It is observed that the deviation of the fatigue life of C1-WCs caused by various lateral boundary conditions is dramatic. The average value of $N_{\mathrm{BC1}}/N_{\mathrm{BC2}}$ of C1-WC is 0.66. In comparison to the “complete tower” conditions (BC2), the laboratory segment fatigue tests are rather conservative for C1-WCs by predicting a fatigue life of −34 % compared to the expected life in a complete tower. The influence of steel strength on their fatigue performance is shown in Fig. 26 (b). Its effect can be neglected as long as a suitable material is selected for connections.

Connections with bolts face a number of difficulties, which may appear during the assembly process or in service [61]. The difficulties include the accuracy of applied bolt force, self-loosening of bolts, and short-term and long-term relaxation of bolts. It is well known that the fatigue performance of RF and RFD connection is very sensitive to pretension force level in bolts. The most optimistic results about bolt force response under the identical nominal stress range can be extracted from the FE simulation. These bolt forces can be used to calculate the fatigue life of RF/RFD connections without imperfections. Fig. 27 shows the discrepancy in fatigue life of connections with four preload coefficients ρ under $\Delta\sigma_{\mathrm{seg}}$ of 127 MPa. It is clearly found that the fatigue performance of RF connections is the most negatively influenced by ρ. On the contrary, C1-WCs show their robust fatigue performance even with varied ρ. The degradation of fatigue life of C1-WCs is 0.13 from $\rho = 0.70$ to $\rho = 0.25$. In other words, the fatigue performance of C1-WCs is insensitive to the variation of bolt preload force which could be generated by the issues mentioned above. However, these issues will lead to huge degradation of the fatigue resistance of RF and RFD connections.

7. Comparison between connections

To compare the performance of connections designed with similar Z_U and Z_I, specimens RF-BC2-S460, RFD-BC2-S460, and WC-BC2-S460 with three different preload coefficients ρ are selected. Table 8 and Fig. 28 illustrate the configuration details and results of the selected specimens. The initial stiffness is obtained by tangential approximation of the load–displacement curve within the critical load Z_I. RFD connections display slightly higher initial elastic stiffness than RF and C1-WCs. Fig. 28 (b) shows RFD-BC2-S460 achieves approximately similar fatigue performance to RF-BC2-S460 with lower bolt preload force (649 kN). The maximum bolt stress in C1-WC is within the elastic range of the

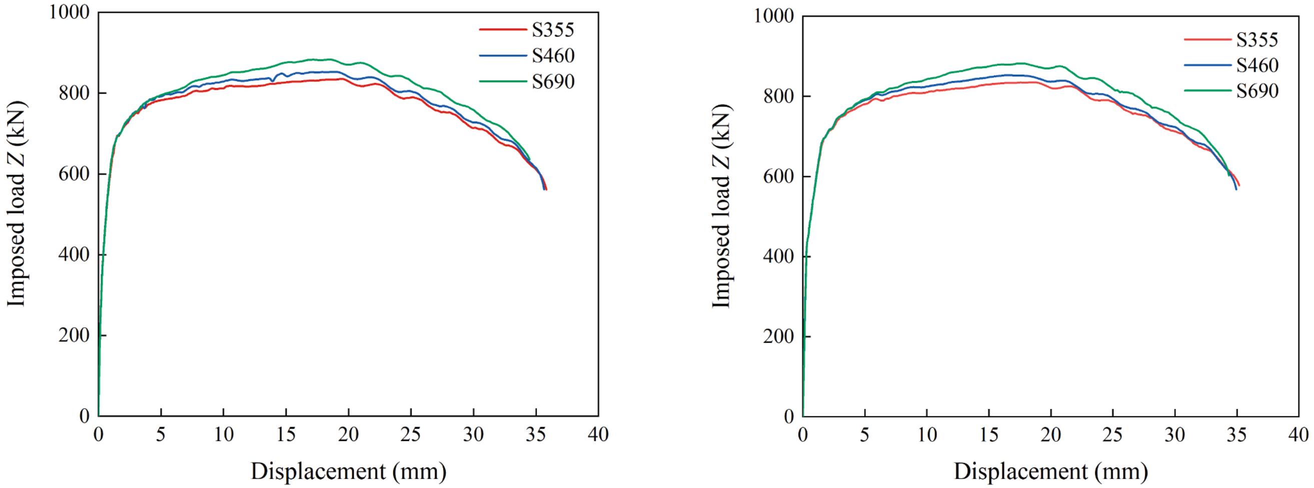

(a) RF-BC2-S355/460/690

(b) RF**D**-BC2-S355/460/690

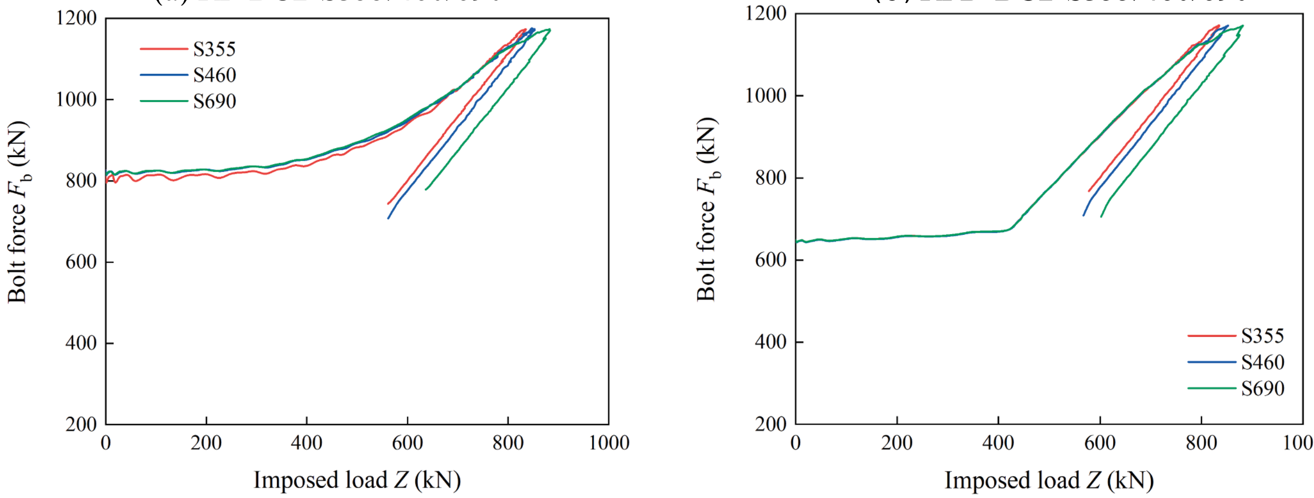

(c) RF-BC2-S355/460/690

(d) RFD-BC2-S355/460/690

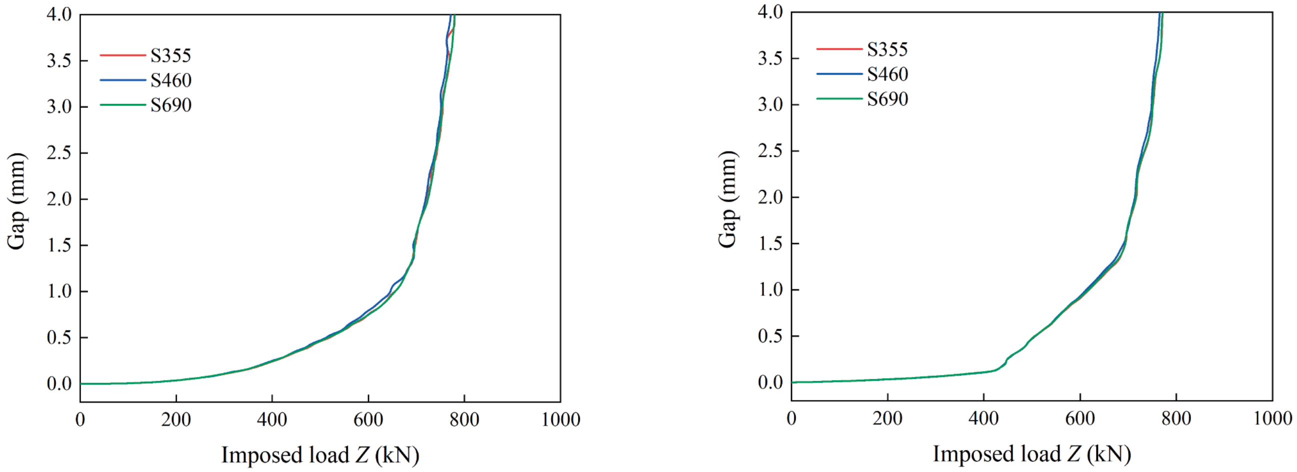

(e) RF-BC2-S355/460/690

(f) RFD-BC2-S355/460/690

Fig. 22. Comparison of RF/RFD connections made of various steel grades: (a) and (b) load–displacement curves, (c) and (d) bolt force evolution curves, and (e) and (f) gap.

bolt (see Fig. 28 (b)). The gap opening at the ultimate state of RF/RFD connections (20 mm) is around six times the one of C1 connections (3 mm), as seen in Fig. 28 (c). Compared to RF/RFD connections, the C1-WC shows the lowest gap before reaching Z_I. It implies that the bolts in the RF/RFD connections could be more prone to corrosion than C1-WC, which may accelerate the fatigue crack initiation and propagation [61].

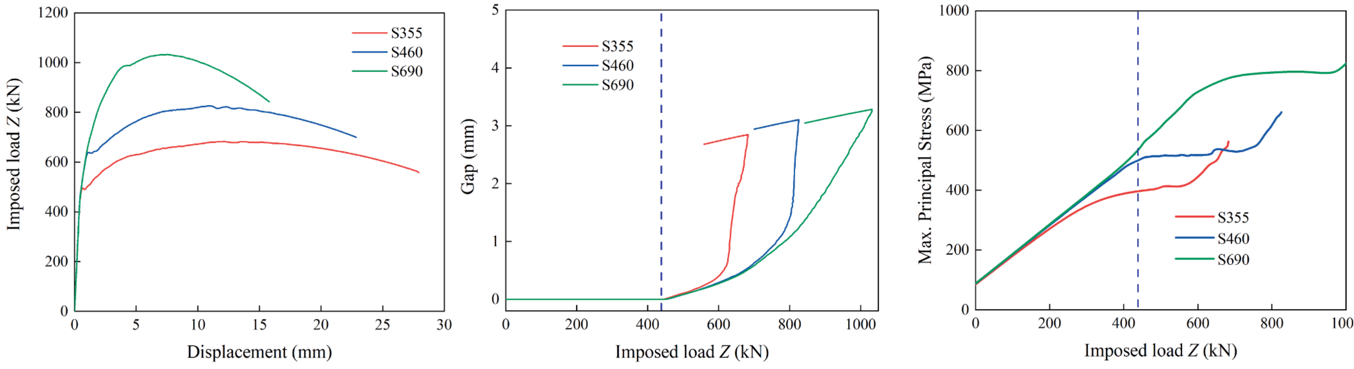

(a) Load-displacement curves (b) Gap (c) Maximum principal stress

Fig. 23. Comparison of C1-WCs made of various steel grades.

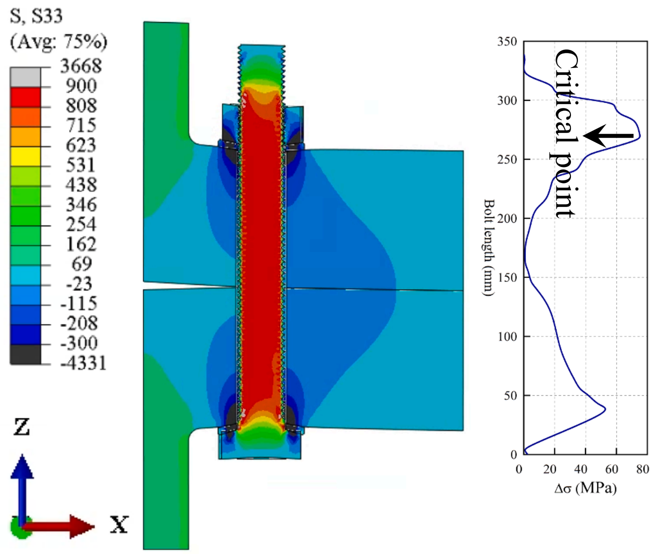

Fig. 24. Critical position in RF-BC2-S460 with $\rho = 0.70$ under $Z = 400$ kN.

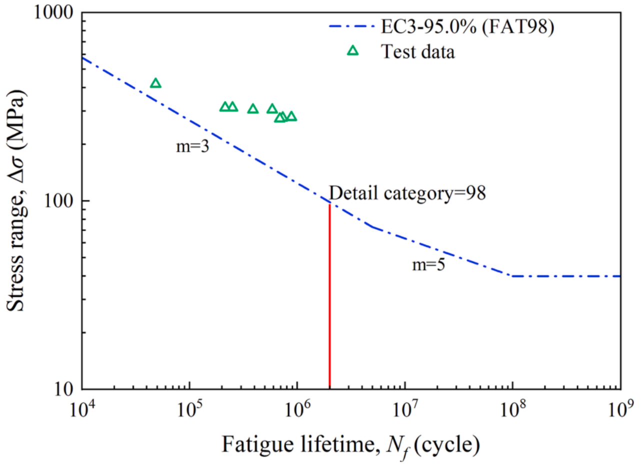

Fig. 25. S—N curves for C1-WCs.

8. Conclusions

This paper provides a comprehensive comparative analysis between three connections for possible use in towers supporting wind turbines, namely bolted ring-flange connection (RF), bolted ring-flange connection with a defined area (RFD), and the C1 wedge connection (C1-WC). Advanced FE models are established and validated against test results. Afterwards, parametric studies on tensile behaviour and fatigue performance are performed to assess the effect of the lateral boundary conditions on the sides of the segment specimen, preload coefficient ρ, and steel strength. The following conclusions are drawn:

Table 6
Determined stress range $\Delta\sigma_{\mathrm{pri,max}}$ (MPa) of C1 WCs for different nominal stress ranges.

ρ	Boundary condition	Nominal stress range $\Delta\sigma_{\mathrm{seg}}$ (MPa)				
		25	51	76	102	127
0.70	BC1	95.4	181.8	274.7	375.1	470.2
	BC2	80.5	155.5	242.7	332.8	403.9
0.55	BC1	93.7	180.1	273.9	373.5	470.4
	BC2	81.5	160.8	245.8	321.7	409.5
0.40	BC1	92.5	178.9	272.5	371.8	462.3
	BC2	81.4	160.9	247.0	323.8	412.9
0.25	BC1	93.0	179.7	270.6	372.5	476.4
	BC2	82.0	161.3	274.8	335.1	424.0

Table 7
Fatigue life N of C1-WCs in number of cycles.

ρ	Boundary condition	Nominal stress range $\Delta\sigma_{\mathrm{seg}}$ (MPa)				
		25	51	76	102	127
0.70	BC1	9.47×10^{6}	1.06×10^{6}	3.07×10^{5}	1.20×10^{5}	6.11×10^{4}
	BC2	2.21×10^{7}	1.69×10^{6}	4.45×10^{5}	1.72×10^{5}	9.64×10^{4}
	$N_{\mathrm{BC1}}/N_{\mathrm{BC2}}$	0.43	0.63	0.69	0.70	0.63
0.55	BC1	1.03×10^{7}	1.09×10^{6}	3.09×10^{5}	1.22×10^{5}	6.10×10^{4}
	BC2	2.08×10^{7}	1.53×10^{6}	4.28×10^{5}	1.91×10^{5}	9.25×10^{4}
	$N_{\mathrm{BC1}}/N_{\mathrm{BC2}}$	0.50	0.71	0.72	0.64	0.66
0.40	BC1	1.10×10^{7}	1.11×10^{6}	3.14×10^{5}	1.24×10^{5}	6.43×10^{4}
	BC2	2.09×10^{7}	1.53×10^{6}	4.22×10^{5}	1.87×10^{5}	9.02×10^{4}
	$N_{\mathrm{BC1}}/N_{\mathrm{BC2}}$	0.53	0.73	0.75	0.66	0.71
0.25	BC1	1.07×10^{7}	1.09×10^{6}	3.21×10^{5}	1.23×10^{5}	5.88×10^{4}
	BC2	2.02×10^{7}	1.51×10^{6}	4.18×10^{5}	1.69×10^{5}	8.34×10^{4}
	$N_{\mathrm{BC1}}/N_{\mathrm{BC2}}$	0.53	0.72	0.77	0.73	0.71

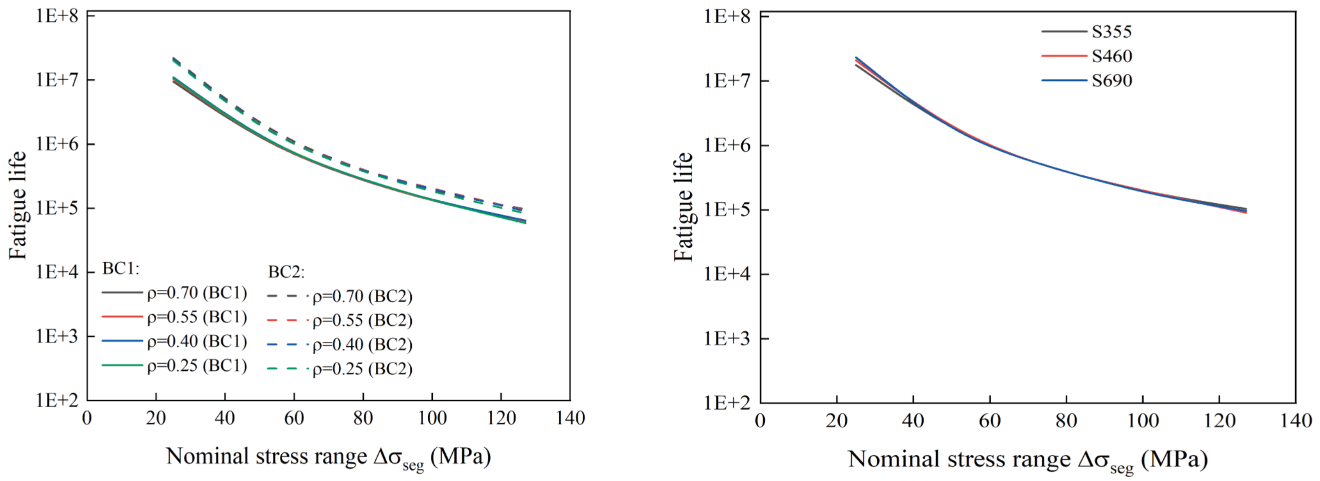

(a) WC-BC1/2-S460

(B) WC-BC2-S355/460/690 with ρ=0.4

Fig. 26. Fatigue life in the number of cycles of C1-WCs with various BC, ρ, and steel strength.

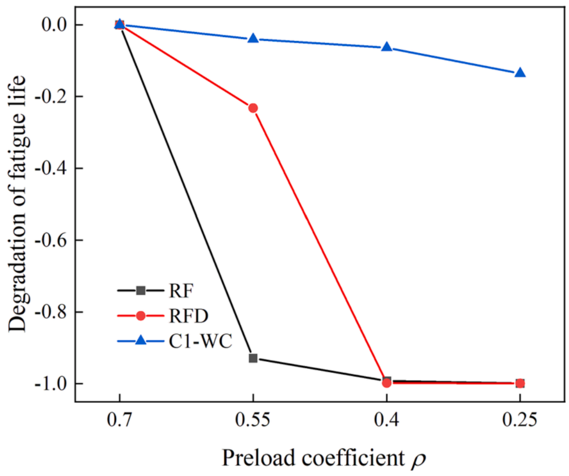

Fig. 27. Degradation of fatigue life.

Table 8
Configuration details of connections with similar Z_U and Z_I.

Specimen	Bolt preload (kN)	Bolt rotation (rad)	Bolt	Initial stiffness (kN/mm)	Z_I (kN)	Z_U (kN)
RF-BC2-S460	825 (0.70A_sf_u)	2.08	M42-10.9	1564	428	853
RFD-BC2-S460	649 (0.55A_sf_u)	1.79	M42-10.9	1743	427	853
WC-BC2-S460	80 (0.40A_sf_u)	29.19	M18-10.9	1183	450	826

(1) The influence of “continuity” conditions, circumferential (hoop) stress, on the tensile static behaviour of RF and RFD connection, is negligible. However, the stress response of crucial components in C1-WCs is significantly influenced by the effect of circumferential stress. It is indicated that the BC1 causes a more uniform distribution of stress response in the C1 WC and a smaller stress concentration factor k_f. Furthermore, the ranges of maximum principal stress $\Delta\sigma_{\mathrm{pri,max}}$ and stress concentration factors k_f of C1-WCs with BC2 are lower than that with BC1.

(2) The reduced pretension level in bolts, given by coefficient ρ, leads to a noticeable reduction of initial stiffness and the critical load Z_I for L-flange connections, while their ultimate capacity Z_U remains constant. The stress response of C1-WCs, for different ρ, depends on the continuity boundary conditions. The stress response of C1-WCs with BC1 is rather consistent under various preload forces (ρ). However, by increasing ρ under BC2, a higher maximum principal stress $\sigma_{\mathrm{pri,max}}$ is generated but with smaller $\Delta\sigma_{\mathrm{pri,max}}$ and k_f. The benefits of a sufficient pretension level under ideal contact alignment are demonstrated for all three types of connections.

(3) Before the bolt yields, the effect of steel strength on the tensile behaviour of RF and RFD connections is negligible. On the contrary, the strength of steel plays a significant role in ultimate limit state of C1-WCs. This indicates the potential of using higher-strength steel in this connection. The recommended yield strength of the steel in the C1-WC should be greater than $Z_I/A_{s,\mathrm{WC}}$.

(4) The effectiveness of the laboratory segment tests for the C1 wedge connection is thoroughly evaluated. The ratio between the fatigue life under BC1 and BC2 ($N_{\mathrm{BC1}}/N_{\mathrm{BC2}}$) for C1 WCs is 0.66. The laboratory segment fatigue tests lead to a rather conservative assessment for C1-WCs.

(5) Under a similar ULS/fatigue load, RFD exhibits higher initial stiffness compared to other connections. Between ρ = 0.70 and 0.25, the degradation of the fatigue resistance of RF/RFD connections is seven times higher than C1-WCs (the lifetime degradation of 0.13). It indicates that the C1 wedge connection is a very robust connection for offshore applications. By omitting the heavy ring flange and employing smaller diameter bolts, the C1-WCs would reduce the fabrication, installation and maintenance costs compared to the traditional RF connections.

Data availability Statement:
The datasets analyzed during the current study are available from the corresponding author upon reasonable request.

CRediT authorship contribution statement

Lu Cheng: Conceptualization, Methodology, Validation, Formal analysis, Visualization, Software, Writing – original draft. **Fei Yang:** Conceptualization, Validation, Supervision, Writing – review & editing. **Marc Seidel:** Writing – review & editing. **Milan Veljkovic:** Conceptualization, Supervision, Writing – review & editing.

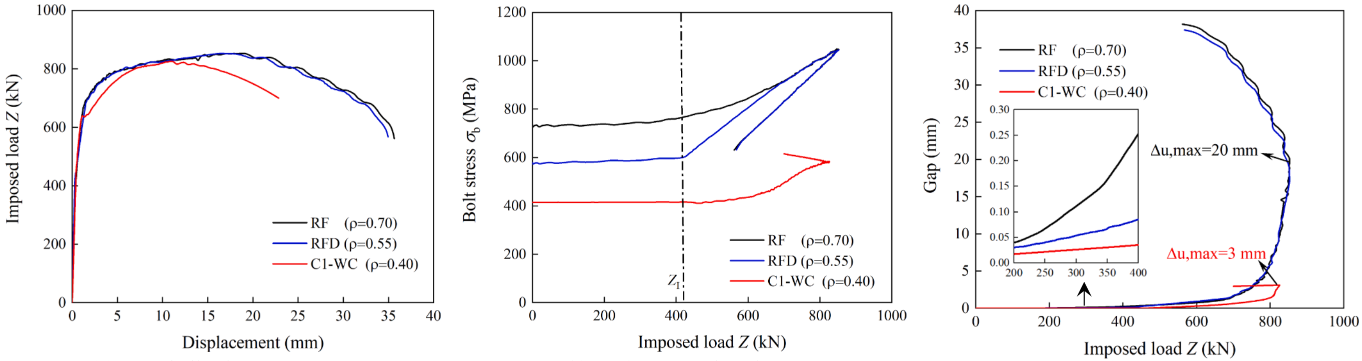

(a) Load-displacement curves

(b) Bolt stress development

(c) Gap

Fig. 28. Comparison between connections with similar Z_U and Z_I.

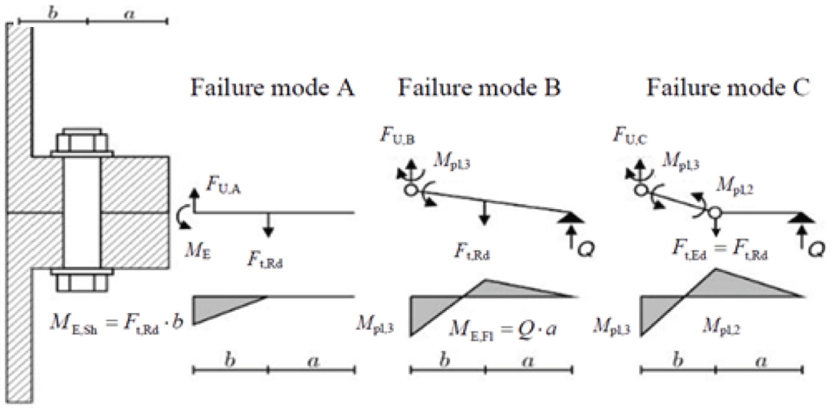

(a) Failure modes A, B, and C [31]

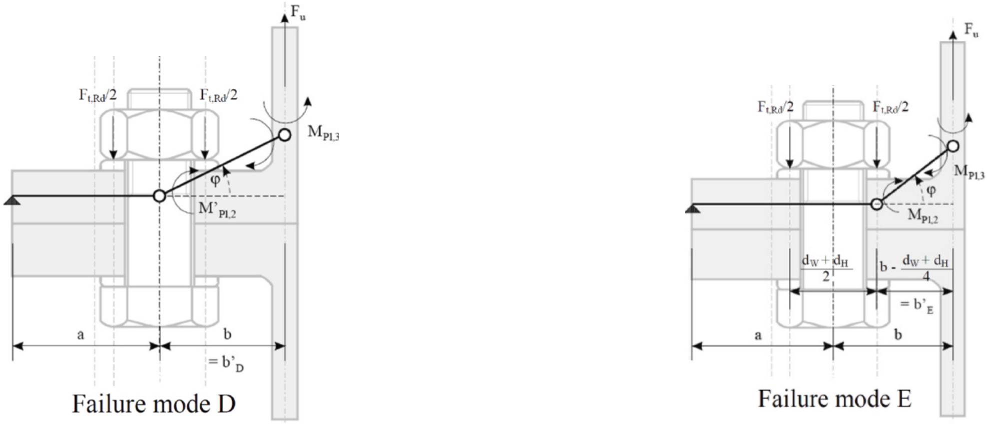

(b) Failure modes D and E [19]

Fig. 29. Failure modes of RF connections.

Declaration of Competing Interest

The authors declare that they have no known competing financial interests or personal relationships that could have appeared to influence the work reported in this paper.

Data availability

Data will be made available on request.

Acknowledgement:

The first author wishes to express gratitude for the financial support of the China Scholarship Council (CSC) under grant number 201806060122. Special acknowledgement is given to Mr Jasper Winkes, Mr Koen Creusen and Mr George Misios from C1 Connections B.V. for sharing experimental data and information about the C1 wedge connection. The authors also would like to thank Mr Peter Vries from TU Delft for sharing the test report about L-flange connections.

Appendix:

Notation in Table 1:

a: the distance from the bolt axis to the flange edge.

b: the distance from the bolt axis to the shell mid plane.

A_s: tensile stress area of bolt.

f_{ub}: the ultimate strength of bolt.

$F_{t,Rd}$: tensile resistance of bolts.

$M_{pl,Rd,sh}$: design plastic bending resistance of shell.

$M_{pl,Rd,fl}$: design plastic bending resistance of flange.

$N_{pl,Rd,sh}$: design plastic resistance of shell.

$V_{pl,Rd,fl}$: design plastic shear resistance of flange.

$M_{pl,Rd,fl,net}$: design plastic bending resistance of net cross-section of flange.

$M_{pl,2}$: full bending resistance of the flange.

$M_{pl,2}$': bending resistance of the flange at the bolt axis.

$M_{pl,3}$: bending resistance considering the M−N and M−V interaction.

References:

[1] Wiser R, Rand J, Seel J, Beiter P, Baker E, Lantz E, et al. Expert elicitation survey predicts 37% to 49% declines in wind energy costs by 2050. Nat Energy 2021;6:555–65. https://doi.org/10.1038/s41560-021-00810-z.

[2] Díaz H, Guedes SC. Review of the current status, technology and future trends of offshore wind farms. Ocean Eng 2020;209:107381. https://doi.org/10.1016/J.OCEANENG.2020.107381.

[3] Liao D, Zhu SP, Correia JAFO, De Jesus AMP, Veljkovic M, Berto F. Fatigue reliability of wind turbines: historical perspectives, recent developments and future prospects. Renew Energy 2022;200:724–42. https://doi.org/10.1016/J.RENENE.2022.09.093.

[4] Soares-Ramos EPP, de Oliveira-Assis L, Sarrias-Mena R, Fernández-Ramírez LM. Current status and future trends of offshore wind power in Europe. Energy 2020;202:117787. https://doi.org/10.1016/J.ENERGY.2020.117787.

[5] Igwemezie V, Mehmanparast A, Kolios A. Current trend in offshore wind energy sector and material requirements for fatigue resistance improvement in large wind turbine support structures – a review. Renew Sustain Energy Rev 2019;101:181–96. https://doi.org/10.1016/J.RSER.2018.11.002.

[6] WindEurope. Offshore wind energy 2022 mid-year statistics 2022. https://windeurope.org/intelligence-platform/product/offshore-wind-energy-2022-mid-year-statistics/.

[7] WindEurope. Offshore wind in Europe - key trends and statistics 2020 2021. https://windeurope.org/intelligence-platform/product/offshore-wind-in-europe-key-trends-and-statistics-2020/.

[8] WindEurope. Offshore wind in Europe - key trends and statistics 2021 2021. https://windeurope.org/intelligence-platform/product/offshore-wind-in-europe-key-trends-and-statistics-2021/.

[9] Bhattacharya S. Challenges in design of foundations for offshore wind turbines. Eng Technol Ref 2014;1:922. https://doi.org/10.1049/ETR.2014.0041.

[10] Petersen C. Stahlbau: Grundlagen der Berechnung und baulichen Ausbildung von Stahlbauten [Steel construction: basics of calculation and structural design of steel structures]. Vieweg; 1993.

[11] Schmidt H, Neuper M. Zum elastostatischen Tragverhalten exzentrisch gezogener L- Stöße mit vorgespannten Schrauben On the elastostatic load-bearing behaviour of eccentrically drawn L-joints with preloaded bolts. Stahlbau 1997;66:163–8.

[12] Seidel M, Stang A, Wegener F, Schierl C, Schaumann P. Full-scale validation of FE models for geometrically imperfect flange connections. J Constr Steel Res 2021;187:106955. https://doi.org/10.1016/J.JCSR.2021.106955.

[13] Weijtjens W, Stang A, Devriendt C, Schaumann P. Bolted ring flanges in offshore-wind support structures - in-situ validation of load-transfer behaviour. J Constr Steel Res 2021;176:106361. https://doi.org/10.1016/j.jcsr.2020.106361.

[14] Krutschinna L. Untersuchungen zum Tragverhalten von Ringflanschsegmenten mit definierten Kontaktflächen [Investigations on the load-bearing behaviour of annular flange segments with defined contact surfaces]. Universität Hannover; 1999.

[15] The C1 wedge connections n.d. https://c1connections.com/ (accessed March 9, 2022).

[16] Creusen KEY, Misios G, Winkes JS, Veljkovic M. Introducing the C1 Wedge Connection. Steel Constr 2022;15:13–25. https://doi.org/10.1002/STCO.202100039.

[17] Nobelwind Offshore Wind Farm, North Sea, Belgium n.d. https://www.power-technology.com/projects/nobelwind-offshore-wind-farm/ (accessed March 9, 2022).

[18] Petersen C. Nachweis der Betriebsfestigkeit exzentrisch beanspruchter Ringflanschverbindungen [Verification of the fatigue strength of eccentrically loaded annular flange connections]. Stahlbau 1998;67:191–203. https://doi.org/10.1002/STAB.199800690.

[19] Seidel M. Zur Bemessung geschraubter Ringflanschverbindungen von Windenergieanlagen [For dimensioning bolted annular flange connections of wind turbines]. Leibniz Universität Hannover 2001. https://doi.org/10.13140/RG.2.2.14685.36328.

[20] DNVGL-ST-0126. Support structures for wind turbines. 2018.

[21] DIN 18088-3. Design standard - structures for wind turbines and platforms – part 3: steel structures. 2019.

[22] VDI 2230 Part I: Systematic calculation of highly stressed bolted joints Joints with one cylindrical bolt. 2003.

[23] IEC 61400-6. Wind turbines – part 6: Tower and foundation design requirements. 2016.

[24] DNVGL. RP-C203: Fatigue design of offshore steel structures. 2014.

[25] Schaumann P, Frithjof Marten D-I. Fatigue resistance of high strength bolts with large diameters. Proc. Int. Symp. Steel Struct. ISSS: Seoul, Korea; 2009. p. 12–4.

[26] Schaumann P, Eichstädt R, Stang A. Advanced performance assessment methods for high-strength bolts in ring-flange connections. Stahlbau 2018;87:446–55. https://doi.org/10.1002/stab.201810601.

[27] Maljaars J, Euler M. Fatigue S-N curves of bolts and bolted connections for application in civil engineering structures. Int J Fatigue 2021;151:106355. https://doi.org/10.1016/J.IJFATIGUE.2021.106355.

[28] Cheng L, Xin H, Veljkovic M. Numerical analysis of ring flange connection with defined surface area. Ce/Papers 2021;4:182–8. https://doi.org/10.1002/CEPA.1279.

[29] Cheng L, Yang F, Veljkovic M. The C1 wedge connection in towers for wind turbine structures, tensile behaviour of a segment test. Eng Struct 2023.

[30] C1 connections obtains DNV certification for the C1 wedge connection^{TM} n.d. https://c1connections.com/news/c1-connections-obtains-dnv-certification-for-the-c1-wedge-connection/ (accessed November 1, 2022).

[31] Petersen C. S. Stahlbau (Steel Construction). Ed Vieweg-Verlag Braunschweig 1997.

[32] Seidel M. Tolerance requirements for flange connections in wind turbine support structures. Stahlbau 2018;87:880–7. https://doi.org/10.1002/stab.201810050.

[33] Wegener F, Seidel M, Glienke R, Marten F, Schwarz M. Numerische Simulation von Vorspannkraftverlusten in Ringflanschverbindungen (Numerical simulation of loss of prestressing force in ring flange connections). Stahlbau 2020;89:1003–15. https://doi.org/10.1002/STAB.202000055.

[34] Pavlović M, Heistermann C, Veljković M, Pak D, Feldmann M, Rebelo C, et al. Connections in towers for wind converters, part I: evaluation of down-scaled experiments. J Constr Steel Res 2015;115:445–57. https://doi.org/10.1016/j.jcsr.2015.09.002.

[35] C1 Connections. Analytical design report-mock-up geometry windpark fryslan loads, 023-003. 2020.

[36] Peter de Vries. L-flange sub-component tests (internal report). 2021.

[37] Simulia.. Abaqus/CAE User's Manual. Version 2016;6:14.

[38] Tobinaga I, Ishihara | Takeshi.. A study of action point correction factor for L-type flanges of wind turbine towers. Wind Energy 2018;21:801–6. https://doi.org/10.1002/we.2193.

[39] Veljkovic M, Feldmann M, Naumes J, Pak D, Simões da Silva L, Rebelo C. Wind turbine tower design, erection and maintenance. Wind Energy Syst. Optimising Des. Constr. Safe Reliab. Oper. Woodhead P, 2010, p. 274–300. Doi: 10.1533/9780857090638.2.274.

[40] International Organization for Standardization (ISO), ISO 4014, Hexagon Head Bolts – Product Grades A and B. 2011.

[41] Deutscher Ausschuss für Stahlbau DASt. DASt-Guideline 021: Schraubenverbindungen aus feuerverzinkten Garnituren M39 bis 72. Düsseldorf: Stahlbau Verlags- und Service GmbH; 2013.

[42] ISO. International Organization for Standardization (ISO), ISO 4017, Hexagon head screws product grades A and B. Switzerland: 2014.

[43] ISO. International Organization for Standardization (ISO), ISO 965–1, ISO General purpose metric screw threads - tolerances. Switzerland: 2013.

[44] EN 1090-2:2008+A1:2011, Execution of steel structures and aluminium structures - Part 2: technical requirements for steel structures. n.d.

[45] EN 10025-6, Hot rolled products of structural steels – Part 6: Technical delivery conditions for flat products of high yield strength structural steels in the quenched and tempered condi-tion. European Committee for Standardization; 2019.

[46] Yang F, Veljkovic M, Liu Y. Ductile damage model calibration for high-strength structural steels. Constr Build Mater 2020;263:120632. Doi: 10.1016/J.CONBUILDMAT.2020.120632.

[47] Ling Y. Uniaxial true stress-strain after necking. AMP J Technol 1996;5:37–48.

[48] Yang F, Veljkovic M, Cheng L. Fracture simulation of fully and partially threaded bolts under tension. Ce/Papers 2021;4:156–61. https://doi.org/10.1002/CEPA.1275.

[49] Kanvinde AM, Asce AM, Deierlein GG, Asce F. Void growth model and stress modified critical strain model to predict ductile fracture in structural steels. J Struct Eng 2006;132:1907–18. https://doi.org/10.1061/ASCE0733-94452006132:121907.

[50] Kanvinde AM, Asce AM, Deierlein GG, Asce F. Finite-element simulation of ductile fracture in reduced section pull-plates using micromechanics-based fracture models. J Struct Eng 2007;133:656–64. https://doi.org/10.1061/ASCE0733-94452007133:5656.

[51] Jia LJ, Kuwamura H. Ductile fracture simulation of structural steels under monotonic tension. J Struct Eng (United States) 2014:140. https://doi.org/10.1061/(ASCE)ST.1943-541X.0000944.

[52] Može P, Yang F, Veljkovic M. Validation and application of bearing and block tearing resistance; background to prEN1993-1-8:2021. J Constr Steel Res 2021;187:106985. https://doi.org/10.1016/J.JCSR.2021.106985.

[53] Ho HC, Chung KF, Liu X, Xiao M, Nethercot DA. Modelling tensile tests on high strength S690 steel materials undergoing large deformations. Eng Struct 2019;192:305–22. https://doi.org/10.1016/J.ENGSTRUCT.2019.04.057.

[54] ISO 898-1. Mechanical properties of fasteners made of carbon steel and alloy steel-Part 1: Bolts, screws and studs with specified property classes-Coarse thread and fine pitch thread (ISO 898-1:2013). Brussels, Belgium: 2013.
[55] EN 1993-1-1: Eurocode 3: Design of steel structures - Part 1-1: General rules and rules for buildings. n.d.
[56] EN 1993-1-9: Eurocode 3: Design of steel structures – Part 1-9: Fatigue. 2005.
[57] DIN 14399-10. High-strength structural bolting assemblies for preloading. British Standard; 2009.
[58] Charlton RS, Eng P. Threaded Fasteners: Part 1 - Failure Modes And Design Criteria of Connections 2011.
[59] Jakubowski A. Ermüdungssichere Bemessung geschraubter Ringflanschstöße in turmartigen Stahlbauten unter besonderer Berücksichtigung von Flanschimperfektionen, [Fatigue Design of Bolted Ring Flanges in Towers with Particular Focus on Flange Imperfection]. Universität Essen, 2003.
[60] Jakubowski A, Schmidt H. Ermüdungssichere Bemessung vorgespannter Ringflanschstöße unter Berücksichtigung von Flanschimperfektionen. Stahlbau 2005;74:452–61. https://doi.org/10.1002/STAB.200590093.
[61] Mehmanparast A, Lotfian S, Vipin SP. A review of challenges and opportunities associated with bolted flange connections in the offshore wind industry. Metals (Basel) 2020;10:732. https://doi.org/10.3390/met10060732.
[62] Buchholz A, Seidel M. Gap height prediction for bolted ring flange connections based on measurements. Steel Constr 2023. https://doi.org/10.1002/STCO.202200019.